ARCHIVIO ISTITUZIONALE DELLA RICERCA

Alma Mater Studiorum Università di Bologna
Archivio istituzionale della ricerca

Pseudomorphic Transformation in Nanostructured Thiophene-Based Materials

This is the final peer-reviewed author's accepted manuscript (postprint) of the following publication:

Published Version:
Zangoli, M., Mazzaro, R., Lunedei, E., Fabiano, E., Manet, I., Candini, A., et al. (2025). Pseudomorphic Transformation in Nanostructured Thiophene-Based Materials. ACS NANO, 19(2), 2245-2260 [10.1021/acsnano.4c11681].

Availability:
This version is available at: https://hdl.handle.net/11585/1011269 since: 2025-03-28

Published:

DOI: http://doi.org/10.1021/acsnano.4c11681

Terms of use:

Some rights reserved. The terms and conditions for the reuse of this version of the manuscript are specified in the publishing policy. For all terms of use and more information see the publisher's website.

This item was downloaded from IRIS Università di Bologna (https://cris.unibo.it/).
When citing, please refer to the published version.

(Article begins on next page)

06 October 2026

ACS NANO

www.acsnano.org

ARTICLE

Pseudomorphic Transformation in Nanostructured Thiophene-Based Materials

Mattia Zangoli,[¶] Raffaello Mazzaro,[¶] Eugenio Lunedei,[¶] Eduardo Fabiano, Ilse Manet, Andrea Candini, Alessandro Kovtun, Meriem Goudjil, Alberto Zanelli, Shlomo Rozen, Massimo Gazzano, Massimo Baroncini,* and Francesca Di Maria*

Cite This: https://doi.org/10.1021/acsnano.4c11681

Read Online

ACCESS | Metrics & More | Article Recommendations | Supporting Information

ABSTRACT: This study reveals the capability of nanostructured organic materials to undergo pseudomorphic transformations, a ubiquitous phenomenon occurring in the mineral kingdom that involves the replacement of a mineral phase with a new one while retaining the original shape and volume. Specifically, it is demonstrated that the postoxidation process induced by HOF·CH_3CN on preformed thiophene-based 1D nanostructures preserves their macro/microscopic morphology while remarkably altering their electro-optical properties by forming a new oxygenated phase. Experimental evidence proves that this transformation proceeds via an interface-coupled dissolution−precipitation mechanism, leading to the growth of a porous oxidized shell that varies in thickness with exposure time, enveloping the pristine smooth core. The oxygenated species exhibits stronger electron-acceptor characteristics than the core material, promoting charge transfer state formation, as confirmed by microspectroscopy and DFT calculations. This enables (i) precise modulation of the nanostructure's surface potential, allowing for the formation of entirely organic heterojunctions with precise spatial resolution via wet chemical processing; (ii) effective doping of the nanostructure, resulting in a strong change of the conductivity temperature dependence and a switch between a low and high conduction state depending on the applied bias. Overall, this work showcases an approach to engineering "impossible" composite architectures with pre-established morphology and tailored chemical-physical properties.

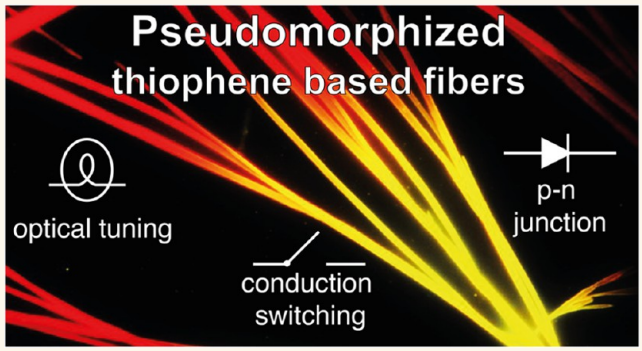

KEYWORDS: *oligothiophenes, crystalline fibers, pseudomorphism, organic heterojunctions, temperature-dependent conductivity*

1. INTRODUCTION

The development of composite materials, featuring the integration of compounds with different functionalities and morphologies, holds considerable promise in an extensive array of current and prospective applications, ranging from biology to electronics.[1−6] By drawing inspiration from natural phenomena, researchers have uncovered innovative processes that enable the realization of increasingly sophisticated multicomponent materials boasting tailored chemical and physical properties. One example of such a phenomenon, ubiquitous in the mineral kingdom, is pseudomorphization.[7−11] This transformative process entails the partial or complete replacement of a mineral phase with a new one when in contact with a fluid, maintaining its original shape and volume.[8] For replacement processes to display fidelity in shape preservation, reactions are often assumed to proceed by solid-state diffusion (*i.e.*, topotactic reactions) or, more commonly, via a tightly coupled dissolution-reprecipitation mechanism at the mineral/fluid interface.[9−11] In the latter case, the spatial and temporal scales of the chemical reactions involved play a pivotal role in dictating the extent to which the original shape of the mineral is preserved.[9−11] By imposing on the new phase the outward crystalline habit of the pristine material, pseudomorphic transformation represents an innovative strategy to generate composite structures featuring distinct phases, each exhibiting unique crystalline architectures and material characteristics. While pseudomorphization has been extensively studied in fields ranging from mineral transformation[12] to the creation of mesostructured silicas,[13−16]

Received: August 23, 2024
Revised: December 23, 2024
Accepted: December 27, 2024

© XXXX American Chemical Society

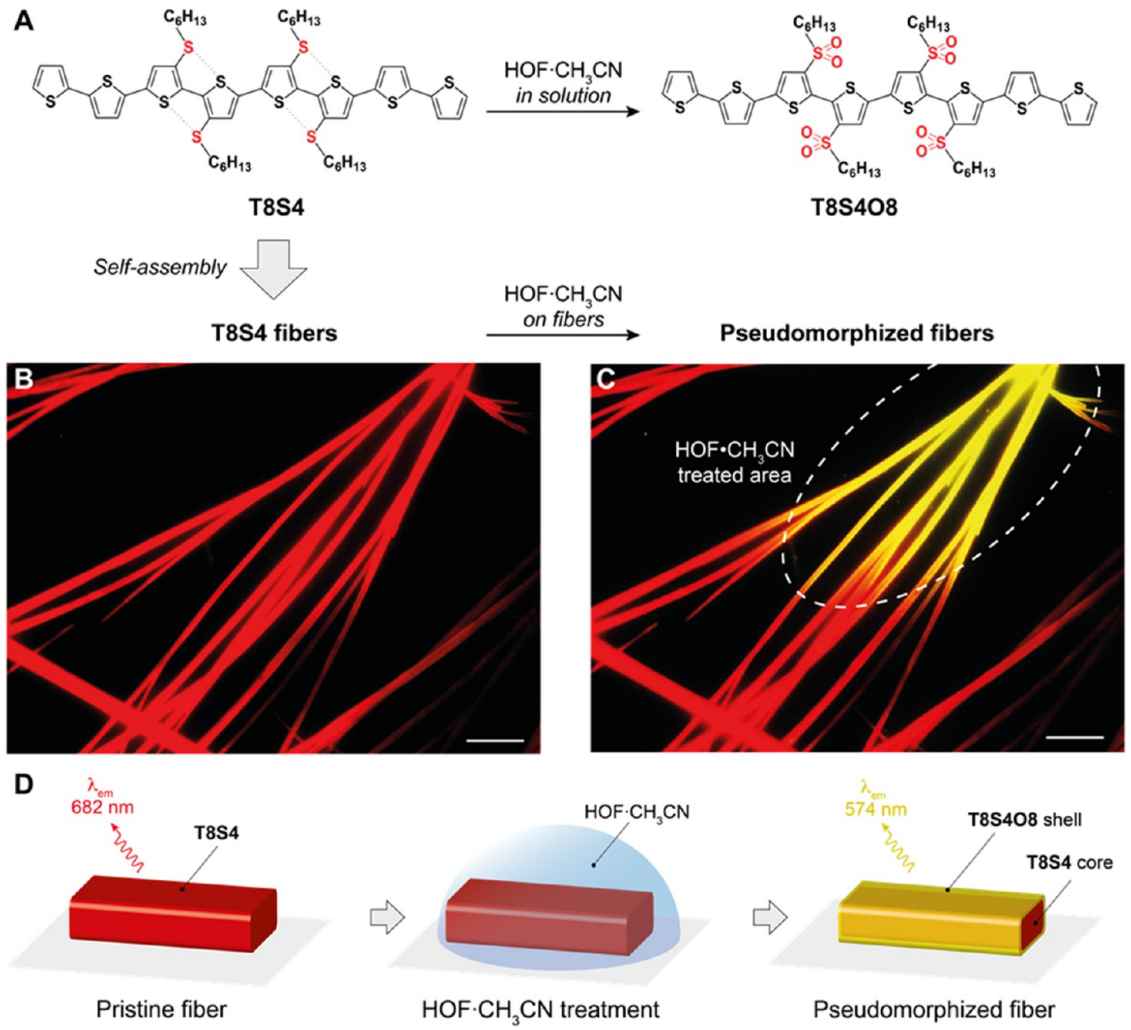

Figure 1. (A) Scheme of the chemical reaction between T8S4 and HOF·CH_3CN in solution, forming T8S4O8. (B, C) Epifluorescence optical micrographs (λ_{ex} = 420 nm) of T8S4 fibers, before and after treatment with HOF·CH_3CN; the treated area is circled by a white dotted line. Scale bars: 25 μm. (D) Schematic representation of the pseudomorphization of a T8S4 fiber.

metal oxides,[17] and metal−organic structures,[18−22] its application in the realm of organic materials remains largely unexplored. Leveraging pseudomorphization in this domain has the potential to yield "impossible" multifunctional/multicomponent organic structures with enhanced performance and functionalities, offering unexplored opportunities for significant breakthroughs in organic electronics, photovoltaics, (bio)sensing, *etc.*

Among organic compounds, thiophene-based materials play a leading role thanks to their unique chemical-physical properties and self-assembly capabilities, hence providing opportunities for the fabrication of tailored supramolecular structures.[23−25] Recent advancements revealed the potential of postoxidation processes on polythiophene-based materials and colloids as a strategy to further tune their characteristics.[26,27] Specifically, Rozen's reagent (HOF·CH_3CN), defined as the most powerful oxygen transfer agent that chemistry has to offer,[28,29] enables the direct chemical transformation of sulfur atoms into S,S-dioxides, leading to significant alterations in the chemical and electronic structure of the resulting material. This includes remarkable changes in the HOMO−LUMO energy levels and the type of prevailing charge carriers (from p- to n-type) in semiconductive thiophene-based materials.[26,27,30−33] However, due to the inherent morphological and dimensional constraints of colloidal nanoparticles (NPs), we were unable to fully elucidate the transformation mechanism, investigate surface potential variations at the junctions, or assess the effects on charge transport characteristics.

Focusing on this, we decided to investigate the postoxidation process in a peculiar class of sulfur-overrich thiophene-based molecules capable of self-assembling into highly crystalline supramolecular nano- and micrometer-sized 1D fibers, characterized by strong fluorescence and charge transport properties.[34−38] We examined the impact of the HOF·CH_3CN treatment on these fibers, particularly those formed by the octamer 3‴,3⁗,4″,4‴′-tetrakis(hexylsulphanyl)-octithiophene,[34] aiming to unravel the changes taking place at the molecular and morphological levels. Through comprehensive analysis and experimentation, we proved that the oxidation process triggers a pseudomorphic transformation of the crystalline fibers, leading to the formation of a nanometer shell composed of a new oxygenated phase enveloping the pristine fibers. We found that this process follows a dissolution-reprecipitation mechanism, resulting in the formation of a crystalline porous shell with a sharp chemical interface. With the aid of density functional theory (DFT) calculations, we

https://doi.org/10.1021/acsnano.4c11681
ACS Nano XXXX, XXX, XXX−XXX

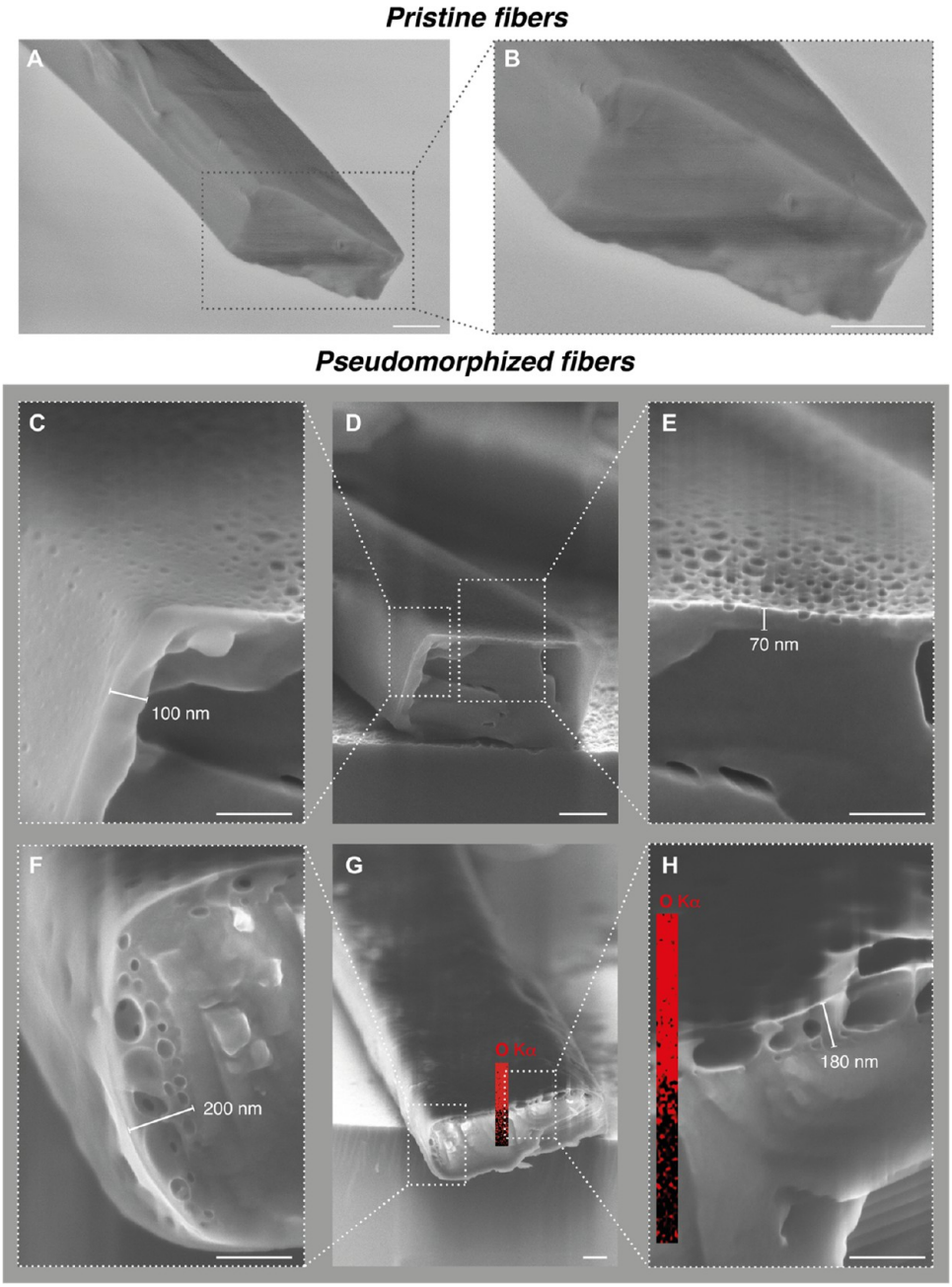

Figure 2. FE-SEM micrographs depicting the cross-section of fibers before (A, B) and after HOF·CH_3CN treatment (C−H). FE-SEM of pseudomorphic fiber cross-section upon exposure to ∼200 μL (C−E) and ∼300 μL (F−H) of HOF·CH_3CN. (G, H) Overlaid EDS mapping of oxygen content on the fiber cross-section details the higher oxygen content in the porous shell. Scale bars: 500 nm (A−G) and 250 nm (C, E, F, H).

elucidated the supramolecular and electronic interactions occurring between the different materials composing the pseudomorphized fibers. In particular, we demonstrated that the pseudomorphization process produces a new material on the fiber surface with an enhanced electron affinity compared with the pristine material, enabling charge transfer (CT) excitations at the junction between the two materials. This allows for finely tailoring the electronic properties of the supramolecular fibers while maintaining control over their crystalline structure and habit. Finally, we showed that individual pseudomorphized fibers (i) present a surface potential curve at the interface between pristine and pseudomorphized regions typical of inorganic p−n junctions; (ii) exhibit switching between high and low conductive states by controlling the bias voltage as a result of the doping effect of the oxygenated shell; and (iii) show photoresponsivity at both room and cryogenic temperatures (40 K). Overall, this study provides a paradigmatic example of a postfunctionalization process, i.e., pseudomorphization taking place on the surface of an organic nanomaterial, to develop innovative multicomponent structures endowed with unique functional properties.

2. RESULTS AND DISCUSSION

2.1. Fiber Formation and Pseudomorphic Transformation. T8S4 fibers were obtained following the methodology described in ref 34. Fibers can be reproducibly grown

https://doi.org/10.1021/acsnano.4c11681
ACS Nano XXXX, XXX, XXX−XXX

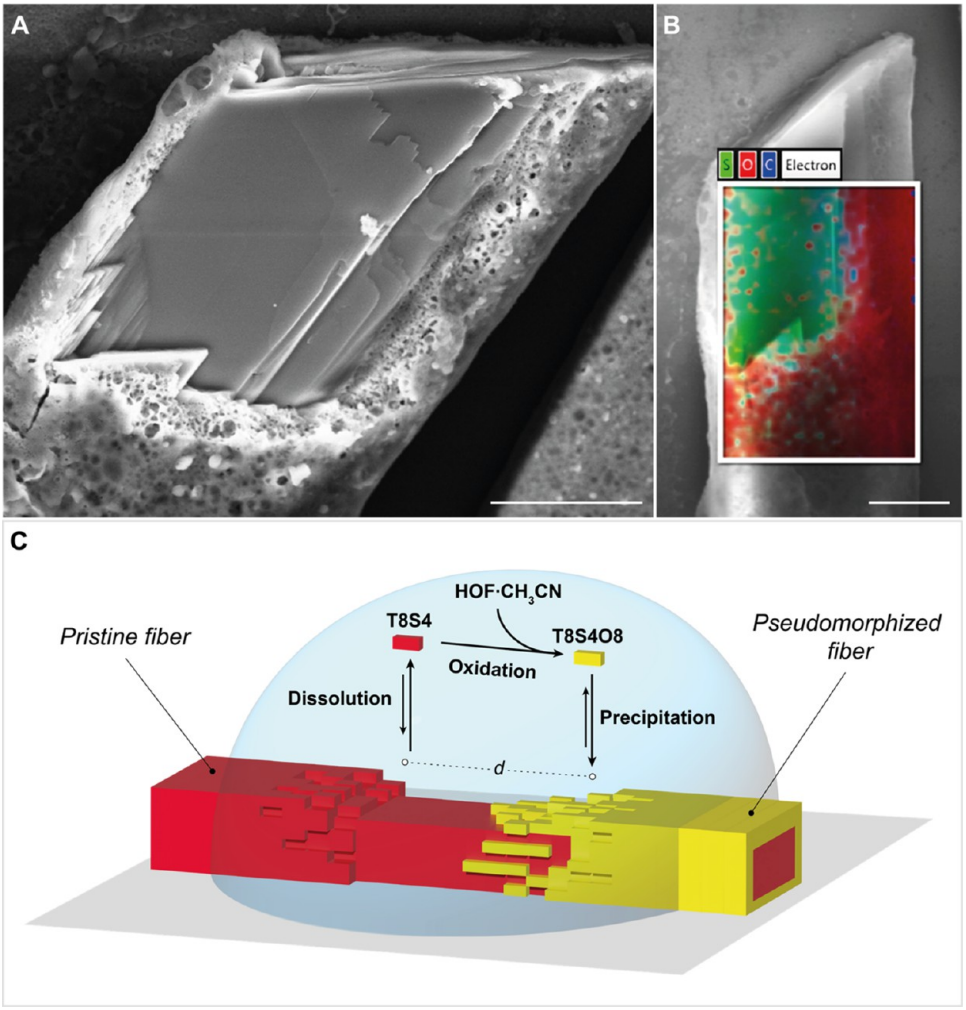

Figure 3. (A) FE-SEM image of a pseudomorphized fiber (treated with ~500 μL of HOF·CH_3CN) whose tip delaminated, highlighting the sharp chemical interface between the core made of T8S4, which presents a smooth and homogeneous surface texture, and the oxygenated T8S4O8 shell, presenting numerous voids distributed throughout the material. Scale bar: 3 μm. (B) FE-SEM image of the same fiber overlapping the distributions of carbon (C), sulfur (S), and oxygen (O) shows that, unlike the surface, the core of the fiber exhibits no signs of oxidation. *Scale bar*: 3 μm. (C) Schematic representation of the dissolution−precipitation mechanism involved in the pseudomorphic transformation of T8S4 fibers.

onto different surfaces (*e.g.*, glass, ITO, SiO_2, etc.) and, in all cases, exhibit (i) high crystallinity; (ii) intense red fluorescence; (iii) high stability; and (iv) sizes extending to millimeters in length and micrometers in width and height.

As summarized in Figure 1, their pseudomorphic transformation can be accomplished by subjecting the fibers to a CH_3CN solution of Rozen's reagent (HOF·CH_3CN) at room temperature (see Section 4 for details). This reagent is a strong oxidant known to promptly oxidize sulfides (C−S−C) to sulfones (C−SO_2−C), hence converting an electron donating group (i.e., sulfide) into an electron acceptor one (*i.e.*, sulfone). In solution, HOF chemoselectively and rapidly oxygenates the aliphatic sulfur atoms of T8S4, forming T8S4O8 (Figure 1A). In the solid state, as shown by optical micrographs (Figures 1B,C and S1), the exposure of preformed fibers to HOF·CH_3CN (see Section 4 for details) in either small or large areas induces a transformative process that preserves their shape and volume while determining a remarkable shift in fluorescence emission, which switches from red to yellow. Furthermore, crossed-polarized micrographs suggest that the treatment does not alter the fiber's crystalline morphology (Figure S1). This indicates that upon evaporation of the CH_3CN solvent, a new oxygenated phase grows on top of the existing T8S4 fibers, mirroring their outward crystalline habit but remarkably altering their physicochemical properties (Figure 1D).

2.2. Composition and Characterization of the Oxygenated Species. The reaction between T8S4 and HOF·CH_3CN was first investigated in a homogeneous solution (Figure 1A). T8S4 dissolved in CH_2Cl_2 upon treatment at room temperature with an excess of HOF (0.4 M) in CH_3CN is instantaneously and chemoselectively oxygenated at the aliphatic sulfur atoms−linked to the β-carbon of the inner thiophenic tetrameric core−forming T8S4O8 in yield exceeding 95%. Synthetic details and ^1H- and ^{13}C NMR characterizations (Figures S2 and S3) are detailed in the Supporting Information. In order to determine the chemical composition of the pseudomorphized fibers, TLC and mass analyses were conducted on T8S4 fibers treated with HOF·CH_3CN after complete solubilization in CH_2Cl_2 (Figures S4 and S5). Analyses consistently revealed that T8S4 persists as the main species, as expected from the larger volumetric size of the unaltered nonoxidized core compared to that of the thin

https://doi.org/10.1021/acsnano.4c11681
ACS Nano XXXX, XXX, XXX−XXX

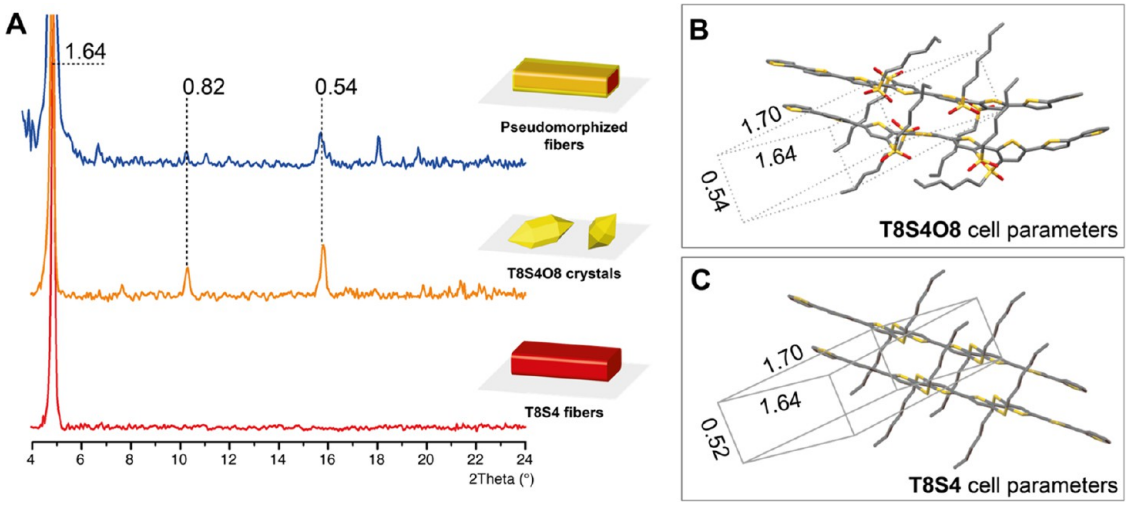

Figure 4. (A) X-ray diffraction patterns of fibers before (red profile) and after (blue profile) treatment with HOF·CH_3CN, compared with the pure cast film of T8S4O8 (yellow profile). (B) Main cell parameters hypothesized for T8S4O8 and measured cell parameters for T8S4,[33] with axis lengths in nm derived from the distances of the main reflections in the X-ray plots.

oxidized shell. The principal oxygenated species identified is T8S4O8 together with trace amounts of a partially oxidized species containing only three aliphatic sulfone groups. The oxygenation of aliphatic sulfur atoms in T8S4O8 induces remarkable variations in the optoelectronic properties of the molecule. A full spectroscopic and electrochemical characterization of T8S4O8 in solution, combined with DFT and TD-DFT calculations, was conducted (details in Supporting Information). In particular, T8S4O8 presents blue-shifted absorption and emission spectra compared to T8S4, consistent with the yellow emission observed in pseudomorphized fibers (Figure S6 and Table S1). Indeed, according to DFT calculations, the 3−3′ regiochemistry of the bulky S,S-dioxide ($-SO_2$) groups in T8S4O8 introduces a distortion of the inner molecular backbone (Figure S7). Furthermore, the high electron affinity of the sulfone groups determines an increase in the charge density on the inner core, depleting the peripheral thiophene units. Thus, stabilizing the HOMO and LUMO energy levels and switching the character of the primary excitation (i.e., mainly a HOMO−LUMO transition) from a pure π- π^*, present in T8S4, to a partially intramolecular CT one in T8S4O8 (Figure S8).

2.3. Morphological Characterization. The morphology of the pseudomorphized fibers was investigated ex situ by scanning electron microscopy (SEM) and compared to that of pristine T8S4 fibers to obtain additional insights into the structural characteristics at the micronanoscale. Figure 2 compares the cross-sectional views of fibers before and after HOF·CH_3CN treatment.

Pristine T8S4 fibers display a compact and smooth surface with a micrometer-sized thickness (Figure 2A,B). Following the oxidation process, fibers maintain their original shapes and proportions (i.e., preserve their solid volume before and after treatment) while exhibiting a nanometer-sized porous shell enveloping the micrometer-sized smooth core (Figures 2C−H and S9). Elemental mapping conducted by SEM energy dispersive spectroscopy (SEM-EDS), in agreement with XPS measurements (Figure S12), confirms that the porous shell is an outcome of the oxidation process which involves only the fibers' outer surface (Figure 2G,H). Indeed, while carbon and sulfur are distributed uniformly across the entire fiber section, oxygen is primarily localized within the nanometric shell and sharply decreases in concentration toward the inner core (Figure S10). Remarkably, the shell thickness results to be directly related to the permanence of the oxidant solution on the fibers. In particular, the longer the exposure time to HOF·CH_3CN, the greater the thickness of the shell and the size of the pores. Consistently, by repetitively adding aliquots of the oxidizing reagent, the shell thickness progressively increases until a complete substitution of the pristine material is achieved (Figure S11). This process is facilitated by the presence of pores, which provide pathways for mass transport,[39] allowing the replacement to proceed toward the innermost layers containing the pristine T8S4 phase. As shown in Figure 3A,B, the delamination of a large fiber highlights a sharp chemical interface between the oxygen-rich oxidized porous outer shell and the unaltered core. The maintenance of the shape and volume of the original fibers, the porous nature of the outer layers, and the sharp chemical interface between the two phases indicate that the transformation process, as observed for inorganic, natural, and artificial systems, occurs via a dissolution−precipitation mechanism.[9−11,39] As sketched in Figure 3C, when crystalline T8S4 fibers come into contact with a CH_3CN solution of HOF, T8S4 molecules from the surface dissolve into the solution, supersaturating the region at the solid−liquid interface. Simultaneously, the dissolved T8S4 molecules undergo a fast and irreversible oxidation reaction with Rozen's reagent, resulting in the formation of oxygenated T8S4 species. The concomitant evaporation of the solvent creates favorable conditions for the epitaxial growth of oxidized products over the existing fibers. Furthermore, the fact that the new phase displays fidelity in shape preservation of the original crystalline fiber indicates that the dissolution−precipitation process, under the employed conditions, remains tightly coupled to the nanometer scale.[39] Notably, conventional oxidants, such as H_2O_2, also yield T8S4O8 in solution, albeit at slower reaction rates (Scheme S1, see the details in Supporting Information). However, subjecting T8S4 fibers to H_2O_2 (30%) does not result in their pseudomorphization (Figure S13), leading instead to the formation of distinct clusters of the oxidized material and partially dissolved fibers.

https://doi.org/10.1021/acsnano.4c11681
ACS Nano XXXX, XXX, XXX−XXX

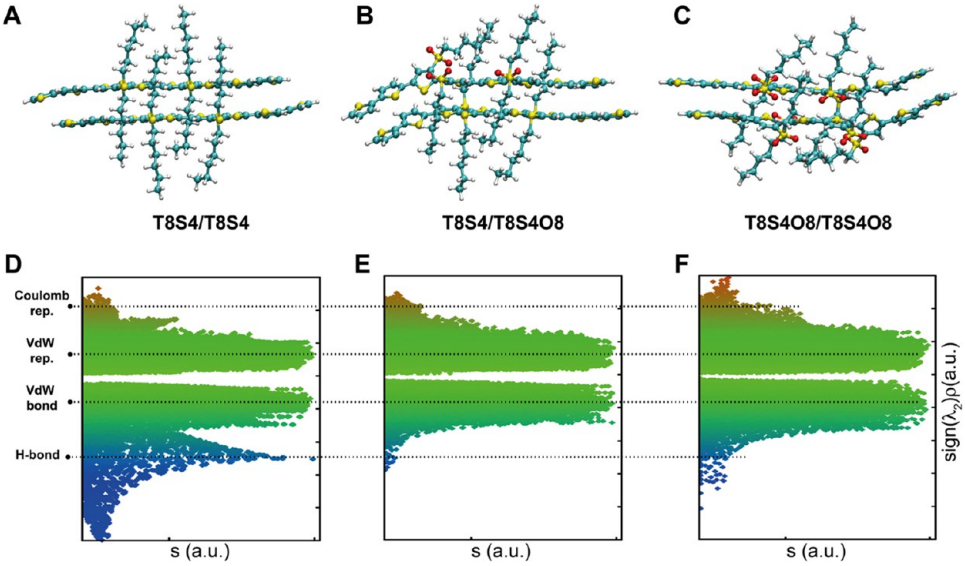

Figure 5. DFT calculated conformations of homo- and heterodimers (A−C) and corresponding noncovalent interaction (NCI) plots (D−F). The NCI plot reports the value of the reduced electron density gradient as a function of the value of the electron density (times the sign of the second density Hessian eigenvalue, λ_2) for every point in the space around the molecule;[37,38] thus, it enables the identification of different noncovalent interactions by the inspection of the peaks in the plot.

This result can be attributed to the slow kinetics of the oxidation reaction of H_2O_2, which facilitates the diffusion of oxidized moieties over larger distances (distance d in Figure 3C) before reaching a state of oversaturation. Consequently, this disrupts the spatial coupling between the dissolution and reprecipitation processes, which is essential for the replacement processes to display fidelity in shape preservation.

2.4. Structural Characterization. To evaluate the effect of the oxidation process on the crystalline structure of pristine T8S4 fibers, powder X-ray diffraction (XRD) analysis was conducted on fiber samples both before and after HOF·CH_3CN treatment (Figure 4).

In addition, examinations were carried out on a pure cast film of T8S4O8 to elucidate its solid-state aggregation characteristics. As depicted in Figure 4A, XRD scans of the different materials are all characterized by a dominant peak at $2\theta = 5.4°$, corresponding to a spacing of 1.64 nm. In pristine T8S4 fibers, this peak is the sole feature within the considered interval due to the high preferential orientation of the sample. As indicated by single crystal determination,[35] it represents the distance between J-stacked molecules in the unit cell depicted in Figure 4C. In cast film of pure T8S4O8, the predominance of the peak at 5.4° suggests a similar crystalline arrangement, but the presence of a further peak at 16.3° and its comparison with the calculated pattern of T8S4 (Figure S14) is indicative of a different crystalline phase. Notably, despite the similarity of the XRD pattern, suggesting an isomorphic structure, T8S4O8 loses the ability to spontaneously organize into fibers, forming crystals with different habits (Figure S15). This can be attributed to the fact that the oxygenation of the aliphatic sulfur atoms inhibits intraintermolecular S···S nonbonding interactions, thus confirming their pivotal role in guiding the organization of this class of materials into fibers.[32−35] Pseudomorphic fibers, in addition to the high-intensity peak at 5.4°, present other lower-intensity peaks at higher theta values (Figure 4A). These additional reflections, some of which coincide with those observed in thin films of pure T8S4O8, provide strong evidence that the oxidized shell maintains a well-defined crystalline order, despite its porosity. By combining XRD data with DFT calculations, we formulated a packing model for the unit cell of T8S4O8. As shown in Figure 4B, the cell parameters were modeled considering the distances of the peaks found in pure T8S4O8 and the spacings in the dimer derived from theoretical calculations.

Through DFT calculations, we investigated homo- and heterodimers constituted by T8S4/T8S4 (i.e., representative of the phase present in the core), T8S4/T8S4O8 (i.e., representative of the interface between the core and shell), and T8S4O8/T8S4O8 (i.e., representative of the outer shell) to elucidate the role of intermolecular interactions established between the different phases present in the pseudomorphic fibers (Figure 5).

In dimers, especially for the T8S4/T8S4O8 heterodimer and T8S4O8 homodimer, the molecular stacking drastically reduces distortions in the inner molecular backbone (the dihedral angle in T8S4O8 decreases up to 25° compared with the monomer), suggesting an almost planar conformation in the solid state (Figure 5A−C). Furthermore, similarly to the monomers, dimers containing T8S4O8 exhibit a pronounced electronic polarization due to the presence of oxygen atoms (Figure S16).

DFT analysis of the interactions among the molecules constituting the dimers highlights relevant differences between the three systems. In particular, the calculated interaction energies (kcal mol^{-1}) show increasing stability in the following order: 67.2 for T8S4/T8S4 < 70.5 for T8S4/T8S4O8 < 77.8 for T8S4O8/T8S4O8. Furthermore, the inspection of electronic properties and the noncovalent interactions (NCI) index aids in distinguishing the nature of the interactions in the different cases.[40,41] In the T8S4 homodimer, the NCI analysis reveals that in addition to the expected VdW contribution mainly due to $\pi-\pi$ interactions and London forces, there is an additional peak at higher density ($\text{sign}(\lambda_2)\rho = -0.025$), which can be attributed to the stronger H-bond interactions originating between the aliphatic sulfur and the hydrogens in the hexyl side chains (Figure 5D). In the T8S4/T8S4O8

https://doi.org/10.1021/acsnano.4c11681
ACS Nano XXXX, XXX, XXX−XXX

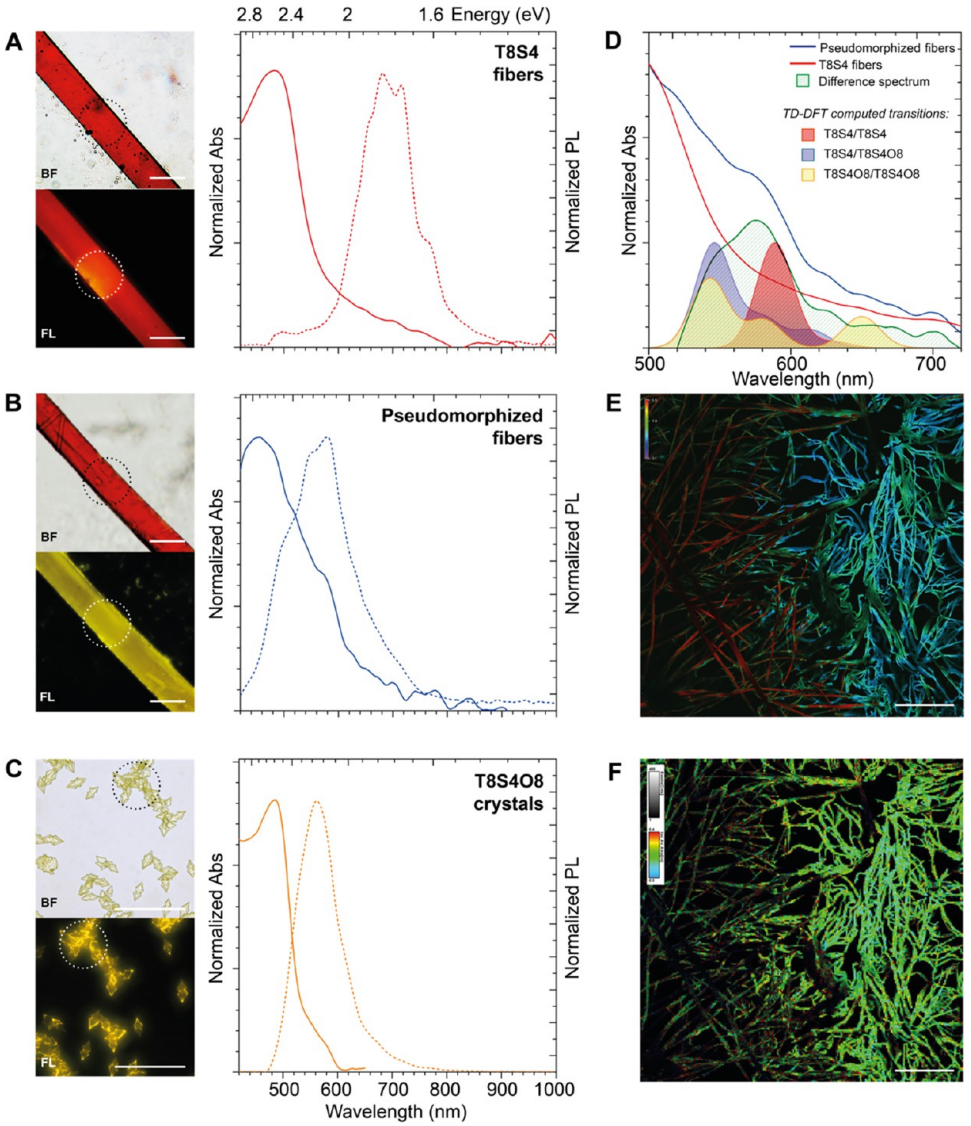

Figure 6. (A–C) Local microabsorption (straight line) and microfluorescence (dashed line; λ_{ex} = 420 nm) spectra of fibers, before and after HOF·CH_3CN treatment, and of pure T8S4O8 crystals collected from the selected area shown in the bright-field and fluorescence microimages on the left (dashed circle, diameter ~30 μm). Scale bars: 5 μm. (D) Absorption spectra differences (green line) between fibers before and after HOF·CH_3CN treatment, overlaid with computed TD-DFT CT transitions of homo- and heterodimers. Confocal fluorescence image of an area displaying two distinct regions within a sample: the untreated area on the left and the treated area on the right, (E) intensity $I_{690\ nm}/I_{585\ nm}$ ratio, and (F) corresponding average fluorescence lifetime images. Scale bars: 25 μm.

heterodimer, the NCI peak relative to H-bonding disappears, in agreement with the fact that the lone pairs of the aliphatic sulfurs are no longer available. Thus, the interaction energy can be traced back mainly to VdW interactions (Figure 5E). Nevertheless, the electronic density distribution analysis indicates that the presence of a permanent dipole moment in T8S4O8 (μ = 10 D) (Figure S8) induces a dipole variation in apolar T8S4 ($\mu \approx 0$ D). This establishes a relatively strong attractive force (permanent dipole–induced dipole) between the two molecules, which results in an increased interaction energy with respect to the T8S4 homodimer. In the T8S4O8 homodimer, once again VdW interactions govern intermolecular bonding (Figure 5F). Furthermore, they are accompanied by a relevant permanent dipole–dipole interaction between the two strongly polar T8S4O8 units. This ensures that despite the increase in steric hindrance generated by the $-SO_2$ groups, the interaction energy in this dimer is the greatest (77.8 kcal/mol), and the distance between the planes of the molecules remains approximately the same as that observed in the other two dimers (~3.4 Å). This analysis suggests that T8S4O8 has a great tendency to form dimers with itself. Based on the proposed mechanism, T8S4O8 nuclei can be preferentially formed once supersaturation conditions are reached. These nuclei can then interact with T8S4 present on the fiber surface due to the high interaction energy observed in the heterodimer (70.5 kcal/mol), thus promoting the epitaxial growth of the oxygenated phase.

2.5. Optical Properties. The optical properties of pseudomorphic fibers were characterized and compared with those of pristine fibers and pure T8S4O8 crystals through optical absorption and emission microspectroscopy.[42] This allows absorption and emission signals to be collected from an area of the crystalline fibers down to 30 μm in diameter. Furthermore, absorption and luminescence were measured (in

https://doi.org/10.1021/acsnano.4c11681
ACS Nano XXXX, XXX, XXX–XXX

transmission mode) across the fibers by collecting the spectrum in various positions to test the homogeneity of the signal. The bright-field and luminescence micrographs, together with their associated spectra, are shown in Figure 6, and the data are summarized in Table S2.

Pristine T8S4 fibers exhibit a broad absorption band peaking at 483 nm (described by HOMO − 1 → LUMO + 1 main single-particle contribution with a dominant $\pi-\pi^*$ character) and a structured emission band centered at 690 nm (described essentially by the LUMO → HOMO single-particle transition, also having a $\pi-\pi^*$ character), which are notably red-shifted compared to T8S4 spectra in solution owing to packing effects (for comparison, see Figures 6A and S6 and Tables S1 and S2).

After treatment with HOF·CH_3CN, the fibers' absorption and emission maxima exhibit a blue shift of approximately 30 and 100 nm, respectively (Figure 6B). The observed shifts match the optical properties of pure T8S4O8 crystals, characterized by sharp absorption and emission spectra with maxima centered at 450 and 540 nm, respectively (Figure 6C).

An in-depth analysis of the absorption spectra of both pristine and pseudomorphized fibers reveals an extended band edge, reaching up to 800 nm in both cases. Furthermore, treated fibers exhibit additional peaks emerging at longer wavelengths, specifically between 500 and 650 nm. According to TD-DFT calculations on model systems based on homo- and heterodimers (Figures S17 and S18), low-energy transitions are responsible for these absorption features. Figure 6D reports the recorded spectra of fibers before and after HOF·CH_3CN treatment, along with their difference, overlaid on the calculated CT transitions of the three dimers. T8S4 homodimer presents a single band near 600 nm, which can be assigned to $\pi-\pi^*$ excitations on both molecules. Differently, T8S4O8 homodimers and T8S4/T8S4O8 heterodimers present multiple bands originating from CT excitations with intra- or intermolecular character. A weak intramolecular CT occurs only in the T8S4O8 molecule and is related to a photoinduced electron transfer from the peripheric thiophene units toward the inner core, in analogy to what is observed in isolated molecules. While, intermolecular CT can occur either between adjacent T8S4O8 molecules in the T8S4O8 homodimer or between a T8S4 molecule and a T8S4O8 molecule in the heterodimer.

To explore the characteristics of fluorescence emissions within the fiber's structure, confocal spectral and fluorescence lifetime imaging (FLIM) was performed. Confocal fluorescence spectra were first measured in different regions of interest (ROI) of partially oxidized samples containing both pristine and pseudomorphized fibers. As shown in Figures 6E and S19, the ratiometric confocal images of the fluorescence intensity at 690 and 585 nm enable a clear distinction between areas composed of pristine and treated fibers, hence offering valuable insights into the extent of the oxidation process. Furthermore, the intensity profiles in Figures S20 and S21 as well as 3D ratiometric imaging in Figure S22 confirm the core−shell structure of the fibers. The fluorescence decay of different selected areas in the images can be fitted satisfactorily with a biexponential decay function. Pristine fibers exhibit an intensity-weighted average emission lifetime of 0.4 ns at 655 nm, characterized by two fitted lifetimes of 0.3 and 1.3 ns (Figure S23). Areas containing treated fibers display an intensity-weighted average emission lifetime of 0.3 at 585 nm, with fitted lifetimes of 0.3 and 1.5 ns (Figure S23). Even if the short lifetime strongly dominates in all cases, it is possible to discriminate areas where oxidation occurred, as they present a shorter average lifetime compared to those in which pristine fibers are present (Figure 6F). Indeed, the relative weight of the preexponential factors of the short- and long-lifetime components of the fluorescence decay allows the identification of the treated region from the untreated region as a result of the increase in the weight of the shorter lifetime in the oxidized fibers (Figure S24). Notably, the pseudomorphization process, while increasing the contribution of the short-time decay component, results in an extension of the long lifetime from 1.3 to 1.5 ns. This observation is consistent with lifetime measurements performed on T8S4O8 crystals, characterized by a lifetime of 0.3 ns fitted by a biexponential decay with components of 0.26 and 1.7 ns (Figure S23).

2.6. Electrochemical Properties. The redox potentials of the pseudomorphized fibers and their separate constituents were investigated through cyclic voltammetry (CV). Figure S25 compares the voltammograms of T8S4 fibers before and after HOF·CH_3CN treatment on indium tin oxide (ITO) current collectors along with the voltammogram of pure T8S4O8. Data are summarized in Table 1.

Table 1. Redox Potentials of Pristine and Pseudomorphic Fibers and T8S4O8[a]

compound	E_{ox}	E_{red}	E_g	HOMO	LUMO
pristine fibers	0.60	−1.52	2.12	5.28	3.16
pseudomorphized fibers	0.79	−1.40	2.19	5.47	3.28
T8S4O8	1.18	−1.27	2.48	5.86	3.38

[a] E_{ox} and E_{red} in V vs SCE were evaluated as onset potential; HOMO, LUMO, and E_g in eV.

The oxidation potential of treated fibers increases by 0.19 V compared to pristine fibers, approaching that of the pure T8S4O8 thin film but still 0.39 V lower (Table 1). This is consistent with the fact that pseudomorphic fibers contain only a nanometer-thick oxidized shell, while the micrometer-sized core remains composed of unaltered T8S4 molecules. An analogous trend is observed for the reduction potential. Treated fibers exhibit a reduction wave of 0.12 V less negative than pristine fibers, in agreement with the increased electron affinity of the oxygenated molecules on the shell. Interestingly, the reduction potential of pure T8S4O8 is found to be −1.27 V, a value of 0.25 V less negative than pristine T8S4 fibers. These data highlight that a staggered alignment of HOMO and LUMO energy levels occurs at the interface between T8S4 and T8S4O8, resembling the characteristics of a type II heterojunction. Furthermore, this alignment results in discernible energy offsets, with Δ_{HOMO} measuring 0.58 eV and Δ_{LUMO} measuring 0.25 eV, which are predicted to provide the necessary driving force for efficient photoinduced charge separation.[43,44] Indeed, it was recently pointed out that a HOMO offset of 0.5 eV is required for efficient nonfullerene-acceptor-based organic solar cells, suggesting that the pseudomorphic fiber can operate as a single crystal heterojunction.[43−45]

Given the relative energetics of the materials constituting the pseudomorphized fibers, it can be anticipated that after the initial generation of charge carriers under an external light stimulus, electrons will transfer toward the T8S4O8 shell while holes remain localized into the T8S4 core, leading to a spatial separation of charge carriers with long-lived interlayer excitons.

https://doi.org/10.1021/acsnano.4c11681
ACS Nano XXXX, XXX, XXX−XXX

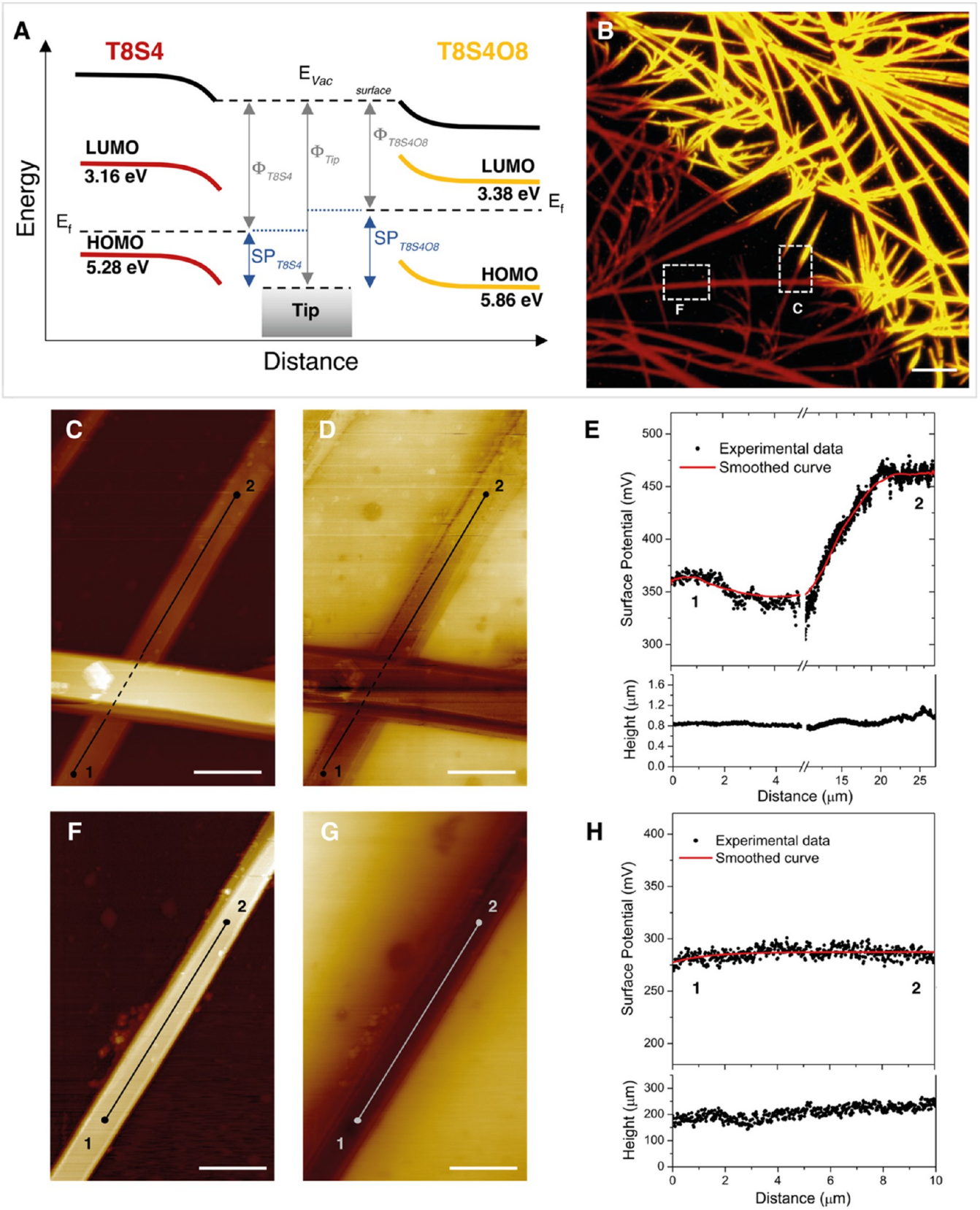

Figure 7. (A) Scheme of the band structure alignment between T8S4 and T8S4O8, depicting SP and work function values. (B) Epifluorescence optical image showing the fibers subjected to KPFM analysis within the dotted square (Scale bar: 25 μm). AFM (C, F) and corresponding KPFM (D, G) images of a partially oxidized fiber (C, D), pristine fiber (F, G), and relative height profile and potential difference along the marked line (E, H). Scale bars: 5 μm.

https://doi.org/10.1021/acsnano.4c11681
ACS Nano XXXX, XXX, XXX−XXX

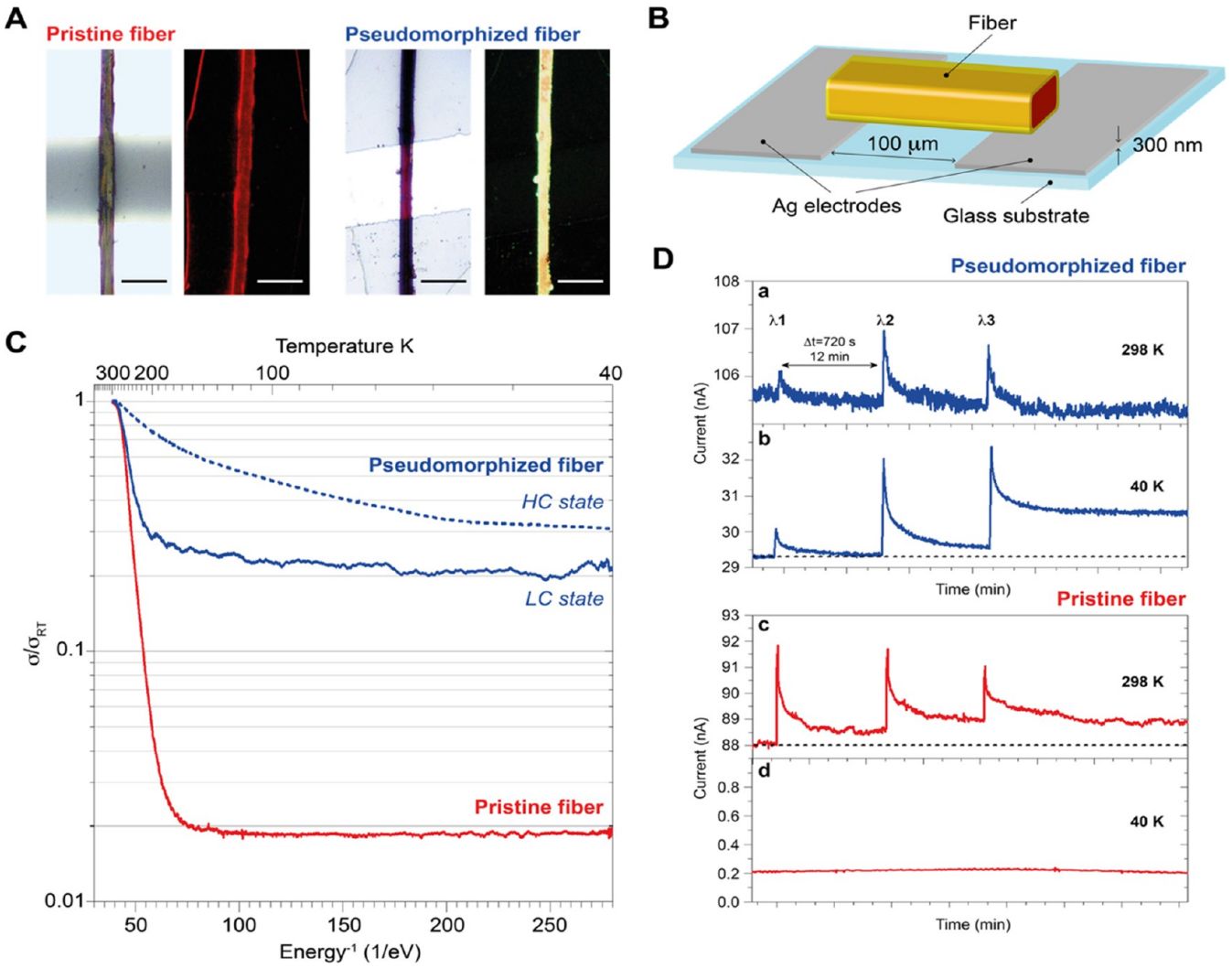

Figure 8. (A) Optical (left) and fluorescence (right; λ_{ex} = 420 nm) microimages of pristine and pseudomorphized fibers mechanically bridging two Ag electrodes (300 nm thick) separated by a 100 μm wide channel under a 1 mm thick transparent PDMS layer to ensure fiber adhesion. *Scale bars*: 50 μm. (B) Schematic experimental geometry used in conductivity measurements. (C) Arrhenius plot: Temperature dependence of the relative conductivity $\sigma(T)/\sigma_{RT}$ (with σ_{RT} room temperature value) for the pristine fiber (red curve) and pseudomorphic fiber in its low (LC, blue straight curve) and high (HC, blue dashed curve) conduction states. (D) Time evolution of photomodulated current across pseudomorphic fibers in HC state (a, b) and pristine fibers (c, d) following the application of a sequence of three 10 s-wide light pulses at intervals of Δt = 720 s, at three different wavelengths (λ_1 = 560 nm, λ_2 = 465 nm, λ_3 = 365 nm), both at T = 298 K and T = 40 K. The operative bias was chosen to ensure a comparable flowing current across fibers (a, b = 10 V, c, d = 50 V).

2.7. Photoinduced Charge Generation. To evidence the possibility for photoinduced charge generation on the surface of pseudomorphized fibers, macroscopic Kelvin probe measurements were carried out both in the dark and under white light illumination (quartz halogen lamp, intensity <0.6 mW/mm^2) on both pristine and treated fiber samples. In dark conditions, treated fibers exhibit a lower (in absolute value) work function (ϕ) than pristine fibers ($\Delta\phi \sim$ 500 meV), meaning that the Fermi level (E_f) is closer to the vacuum level. This is indicative of an increased n-type semiconducting characteristic of the fiber's surface (Table S3). Remarkably, under light illumination, only pseudomorphic fibers show a variation in surface potential (30 mV) (Figure S26), due to a buildup of photogenerated charges on the surface, in agreement with the energetic of the different materials. The variation in surface potential (SP) along single fibers, whether treated or untreated, was further investigated using atomic force microscopy (AFM) and KP-force microscopy (KPFM). Fibers have thicknesses ranging from hundreds of nanometers to 2 μm and exhibit different contrasts in the Kelvin probe image depending on their treatment status. Specifically, pristine fibers present typical surface potential (SP) values ranging from approximately ~250 to ~400 mV, significantly lower than those of treated fibers, usually displaying SP values ~100 mV higher. These findings align well with the trend obtained from macroscopic KP measurements (Table S3). The discrepancy in $\Delta\Phi$ values between macroscopic KP and microscopic KPFM can be attributed to differences in sample thickness since KP examines thick coatings while KPFM analyzes individual fibers.[46−48]

Combining the data from KPFM and CV, the band structure alignment was derived as schematized in Figure 7A. This configuration corroborates the theoretical prediction that in T8S4/T8S4O8 heterostructures, photogenerated electrons are transported from T8S4 to T8S4O8.

https://doi.org/10.1021/acsnano.4c11681
ACS Nano XXXX, XXX, XXX−XXX

Additionally, in Figure 7 are reported the topography and corresponding SP along a partially pseudomorphized fiber (Figures 7C–E and S27) and a pristine one (Figure 7F–H). Interestingly, while there are no discernible differences in the fiber topography between pristine and treated fibers, the SP value significantly increases when passing from the unoxidized to the oxidized region. Remarkably, the observed line profile closely resembles the characteristic sigmoid curve typically associated with p–n junctions in inorganic materials,[49−51] a hallmark of efficient charge separation and transport mechanisms.

2.8. Temperature-Dependent Conductivity and the Photomodulation Effect in Single Fibers. The presence of CT states suggests that at the interface between the core and the shell of the pseudomorphized fibers, the frontier molecular orbitals of T8S4 hybridize with those of T8S4O8 forming a new set of occupied bonding and empty antibonding orbitals (Figure S17). In analogy to what is observed in doped thiophene-based semiconductors, the CT states generated at the T8S4 fibers interface may induce modification of the density of states, hence influencing charge transport properties.[52−55] T8S4O8 being an electron acceptor toward T8S4 can act as a molecular p-dopant.[52−56] Temperature-dependent transport measurements (from 300 to 40 K, in vacuum under darkness) were performed on individual pristine and pseudomorphic crystalline fibers mounted onto Ag electrodes (Figure 8A) in an experimental configuration detailed in Figure 8B.

Figure 8C shows the temperature dependence of the relative conductivity $\sigma(T)/\sigma_{RT}$ (with σ_{RT} being the conductivity value at room temperature) of pristine and pseudomorphic fibers revealing significant differences in their charge transport behavior. Pristine fibers ($\sigma_{pristine}$ at 298 K ~8×10^{-7} S/cm) exhibit a dependence with temperature proper of semiconducting thiophene-based materials,[57] with a characteristic exponential decay and an activation barrier of $E_a \approx 180$ meV, down to around $T \approx 200$ K (typical of hopping mediated conduction). However, beyond this threshold, the conductivity starts to show only a very weak temperature dependence, suggesting a transition to a different conduction regime with low intrinsic mobility.[57] This behavior was observed to be independent of the value of the bias applied during the temperature scan (voltages up to many tens of volts were used). Unlike pristine fibers, transport measurements on freshly prepared pseudomorphized fibers are, in contrast, strongly bias-sensitive. Even if their temperature-dependent relative conductivity (σ_{pseudo} at 298 K ~4×10^{-8} S/cm) shows a general trend similar to that of pristine fiber, a lower activation energy is observed ($E_a \approx 100$ meV), above 200 K. Furthermore, below 200 K, the decrease in relative conductivity (of about factor 5) is rather modest in comparison to that exhibited by pristine fibers (nearly 50 times). We indicate this as the Low Conduction (LC) state of pseudomorphized fibers. The LC state was observed for applied bias up to ~5 V. However, upon biasing the pseudomorphized fibers at only slightly higher voltages (~7–10 V), an abrupt switching to a new High Conduction (HC) state was observed.

This switching was observed to occur at both room and low temperatures. In the HC state, the room temperature conductivity increases by around 3–4 orders of magnitude (σ_{pseudo} at 298 K ~2×10^{-4} S/cm). In the HC state, the relative conductivity of pseudomorphic fiber was observed to decrease slowly but continuously with temperature down to 40 K (Figure 8C). It presents shallow conduction barriers (14 meV < E_a < 1 meV), indicating the existence of transport mechanisms different from that of both pristine and pseudomorphized fibers in the LC state. Notably, the LC state can be restored by discharging the HC fiber for a prolonged time (Figure S28), indicating the full reversibility of this effect and ruling out any irreversible structural alteration of the crystalline fibers. This conductivity change between HC and LC states can be tentatively interpreted as an effect of the electrochemical population of energy states present at the interface between the T8S4O8 oxygenated molecular shell and the crystalline T8S4 core.[58,59]

It was also found that the current flowing across the two different types of fibers is strongly dependent on the application of light excitation (Figure 8D). Pristine and pseudomorphic fibers in the HC state were subjected to short light pulses (10 s) at different wavelengths (560, 465, and 365 nm) at 298 and 40 K. While pristine fibers show photomodulation only at 298 K but not at 40 K (Figure 8D(c,d)), pseudomorphic fibers in the HC state exhibit detectable photomodulation at both temperatures (Figure 8D(a,b)), albeit with a faster relaxation behavior at 298 K indicative of the presence of a larger number of deactivation pathways. Furthermore, pseudomorphic fibers at 40 K show extremely long relaxation times following light excitation, resulting in persistent photoactivated conductivity (Figure 8D(b)). This behavior, which has been previously observed in polymeric thin films,[60,61] is likely caused by the slow recombination of well-separated holes and electrons. This is facilitated by the presence of strongly electron-accepting T8S4O8 molecules at the fiber surface, which promote the creation of electron-trapping states, thus disfavoring fast recombination processes. Conversely, the longer relaxation time observed for pristine fibers can likely be attributed to their higher crystallinity (as a result of the absence of the porous oxygenated shell).

Despite further studies will be needed to fully elucidate this unprecedented behavior, the experimental results reported here are a clear indication of the strong effect that pseudomorphic transformation can have on transport properties, suggesting their potential application in voltage-controllable memory devices.[62]

3. CONCLUSIONS

In this study, we unveiled the occurrence of pseudomorphic transformation, a phenomenon typically observed in the mineral kingdom within the realm of organic materials. In particular, we demonstrate that thiophene-based supramolecular structures, such as fibers made of a sulfur-overrich octathiophene, can be pseudomorphized through treatment with a strong oxidizing reagent, namely, Rozen's reagent. This transformative process results in the formation of multicomponent materials characterized by a nanometer-scale oxidized shell that envelopes the pristine preform with precise spatial confinement. Our results reveal that this transformation occurs via a tightly coupled dissolution-reprecipitation mechanism, enabling the new materials to grow with the same shape and volume as the pre-existing material and to partially or entirely substitute it. It is worth noting that attempts of pseudomorphization with oxidants, such as H_2O_2, are not effective, highlighting the unique efficacy of Rozen's reagent in this process. Through a comprehensive approach,

https://doi.org/10.1021/acsnano.4c11681
ACS Nano XXXX, XXX, XXX–XXX

combining different characterization techniques and theoretical calculations, we provide an insight into the properties and functionalities of these organic multicomponent structures. The increased electron affinity of the oxygenated material promotes the generation of CT states and establishes a staggered alignment of energy levels, thus facilitating efficient charge separation under light illumination. We demonstrate that pseudomorphization can lead to the formation of fully organic p-n heterojunctions at the interface between the pre-existing material and the newly formed oxygenated phase. Furthermore, we show that the oxygenated shell exerts a p-doping effect on the T8S4 core, allowing access to a high-conductivity state that can be switched to a low-conductivity state—characterized by markedly different temperature-dependent transport characteristic—by simply controlling the bias voltage, paving the way for applications in switchable memory devices. Overall, our findings highlight the potential of pseudomorphization for tailoring organic multicomponent nanomaterials with complex morphology and chemistry offering a strategy for the miniaturization of optoelectronic and photovoltaic devices. Lastly, given Rozen's ability to oxidize several functionalities—such as alkenes, alkynes, aromatic hydrocarbons, alcohols, amines, and phosphorus and sulfur-containing substrates—this strategy has the potential to be expanded to a vast pantheon of organic materials.

4. MATERIALS AND METHODS

4.1. Sample Preparation. T8S4 fibers were prepared according to the vapor diffusion method,[34] in which a solution of T8S4 in a good solvent (toluene) at a concentration of 10^{-3} M is exposed to the vapor of a poor solvent (acetonitrile). Once formed on the appropriate substrate (*i.e.*, glass, silicon, and ITO), the pseudomorphization process is conducted by directly treating the fibers with a solution of HOF·CH_3CN. The oxidant was prepared according to the procedure reported in refs 26−30. In a substrate with a fiber-covered area of 1 cm^2 (or 4 cm^2), ∼25 μL (∼100 μL) of a HOF solution (∼0.4 M) was drop-cast and evaporated at room temperature under a nitrogen atmosphere. Additional aliquots were subsequently added to increase the shell thickness.

4.2. Cyclic Voltammetries (CVs). CVs have been performed at room temperature with an AMEL 5000 Electrochemical System in a homemade three-compartment cell with Pt wire counter electrode and aqueous KCl saturated calomel electrode (SCE = −0.50 V vs ferrocene/ferricinium, FC/FC^+). Supporting electrolyte was propylene carbonate (Sigma-Aldrich, anhydrous 99.7%) and 0.1 M $(C_2H_5)_4NBF_4$ (Sigma-Aldrich for electrochemical analysis ≥99.0% stored under dry reduced pressure) carefully purged with Ar before the potential scan at 0.1 V s^{-1}. Fibers were grown on ITO current collectors and subjected to pseudomorphization with HOF·CH_3CN to achieve a nanometric shell of ∼100 nm thick (ITO substrate, area 4 cm^2, HOF·CH_3CN ∼100 μL).

4.3. Scanning Electron Microscopy (SEM) Analysis. Field-emission scanning electron microscopy was performed on a Zeiss LEO 1530 FE-SEM equipped with an X-act 10 mm^2 SDD EDS Detector by Oxford Instruments. Images were collected operating at V_{acc} = 5 keV. Fibers were grown on Si/SiO2 wafers (area 1 cm^2), treated with multiple aliquots, each of ∼25 μL, of HOF·CH_3CN, and dried under vacuum without further treatment. The cross-section was prepared by cleaving the Si/SiO2 wafers, thereby exposing the fiber section at the cleavage site.

4.4. X-ray Photoelectron Spectroscopy (XPS). XPS spectra were recorded by using a Phoibos 100 hemispherical energy analyzer (Specs) with Mg Kα radiation ($\hbar\omega$ = 1253.6 eV). The X-ray power was 125 W. The spectra were recorded in constant analyzer energy mode with analyzer pass energies of 40 eV, which correspond to 1.5 eV energy resolution. Charging effects were corrected by energy calibration on C 1s at 285.0 eV. The base pressure in the analysis chamber during analysis was 5×10^{-8} mbar. Fibers samples, deposited on a silicon substrate (area of 1 cm^2) and subsequently exposed to HOF·CH_3CN (∼25 μL), were put in a high vacuum overnight before measurement.

4.5. X-ray Diffraction (XRD) Analysis. XRD was performed using a PANalytical X'Pert diffractometer equipped with a copper anode (λ_{mean} = 0.15418 nm) and a fast X'Celerator detector. Data were collected with 0.05° steps, counting 50 s at each step. Samples were supported on glass coverslips (area = 4 cm^2) and subsequently exposed to HOF·CH_3CN (∼100 μL). The background due to the glass was cleaned out before plotting.

4.6. DFT Calculations. All calculations have been performed at the PBE0/def2-TZVP level of theory[63,64] using the TURBOMOLE program package v7.7.[65] Only for geometry optimizations we used instead the PBE functional.[66]

4.7. Single Fiber Optical Absorption and Emission Microspectroscopy. Differential reflectance, absorption, and emission spectra of single fibers, both before and after HOF treatment as well as their fluorescence images, were recorded by means of a modified Nikon Eclipse80i epifluorescence microscope. Samples were deposited on glass substrates with an area of 4 cm^2 and treated with ∼100 μL of HOF·CH_3CN. Its standard trinocular turret was customized, in its superior part, in order to mount a homemade optical system (composed of a 50 mm focal quartz lens focused into a UV−vis/NiR optical fiber (200−2200 nm), 550 μm core, Thorlabs) to feed the optical signal from the microscope into an Avantes AvaSpec-2048 CCD spectrometer (2048 pixels array, DLC UV/vis, 200−1100 nm range, 10 or 100 μm entrance slit, software programmed). This allowed us to record fluorescence images and collect the reflected or emitted (for photoluminescence) signal from fibers under a 20−100× objective. In reflection (or transmission) mode, the built-in Nikon top (or bottom) halogen lamp was used (white light, illumination range 380−1200 nm). The lamp light reflected by the sample's surface (or passed across it) was then collected through the microscopy objective and fed into the spectrometer fiber. Furthermore, for the photoluminescence spectra, a top-mounted OSRAM Mercury Short Arc lamp (HBO) 100 W was properly energy filtered to provide a suitable excitation (λ_{exc} = 546 nm), and its light was brought to excite fibers across the microscope objective. The fluorescence signal collected back across the same objective was eventually fed into the spectrometer via an optical fiber after having passed through a dichroic mirror and an exit filter to suppress residual excitation straylight. In this way, it was possible, within the same experimental session, to select the more suitable fiber samples by visual inspection under strong magnification, then record a bright-field microimage, followed by a fluorescence image, and successively measure the local microabsorption via differential reflectance or transmission mode and the local microfluorescence spectrum. Fluorescence images were collected by means of a Nikon DigitalSight DS-2 M camera using a 546 nm excitation filter, a 570 nm dichroic mirror, and a 590 nm long-pass exit filter. Integration time was on the order of a few seconds (0.1−5 s) for the differential reflectance/absorption spectra and between 1/10 and 8 s for fluorescence images.

4.8. Confocal Fluorescence Imaging. Fluorescence confocal imaging was performed on an inverted Nikon Ti-E microscope (Nikon Co., Shinjuku, Japan). The Nikon A1 confocal fluorescence microscope is equipped with an argon ion CW laser as well as 485 nm pulsed/CW diode lasers (PicoQuant GmbH, Berlin, Germany). Images were collected using either a Nikon Plan Apo VC 20× air objective with NA of 0.8 or a Nikon Plan Apo VC 60× oil immersion objective with NA of 1.40. Filters were set to register the fluorescence in the 510−540, 555−615, and 665−735 nm ranges. Nikon A1 spectral module with a precisely corrected 32-PMT array detector is used for spectral imaging. Wavelength resolution was set to 2.5 or 6 nm per PMT.

Fluorescence lifetime imaging was performed by exciting with a pulsed 485 nm diode laser and collecting photons at 520 nm with integrated PicoHarp 300 electronics (PicoQuant GmbH, Berlin, Germany) for TCSPC measurements. Histograms of collected

https://doi.org/10.1021/acsnano.4c11681
ACS Nano XXXX, XXX, XXX−XXX

photons consist of 1600 channels, each with a 16 ps width. A single photon avalanche diode detector equipped with a band-pass filter was used as a detector. The repetition rate of pulsed excitation was 40 MHz. The instrument response time of the system is approximately 220 ps. The fluorescence decay fit was performed on the histogram calculated for a region of interest of the PS fibers in the sample image. The fluorescence decay profile was analyzed with a least-squares method using biexponential decay functions provided by Picoquant SymPhoTime software. The calculated instrumental response function was used for reconvolution. Eventually, the average fluorescence lifetime image was calculated by fixing the lifetimes obtained from the histogram analysis of the region of interest, while the software calculated the pre-exponential factors for each pixel. Pristine fiber samples grown on glass (area 4 cm^2) were partially treated (on an area of about 2 cm^2) with ~50 μL HOF·CH_3CN to obtain sharp boundary zones between oxidized and nonoxidized fibers.

4.9. Time-Correlated Single Photon Counting. Fluorescence decays in air-equilibrated solution and solid were measured for excitation at 465 nm (Horiba led) using an IBH 5000F time-correlated single photon counting system (TCSPC) (IBH Consultants Ltd., Glasgow, U.K.) with a resolution of 55 ps per channel. Photons were detected in right angle configuration with a cutoff filter. Fluorescence decay profiles were analyzed with a least-squares method, using multiexponential decay functions (eq 1) and deconvolution of the instrumental response function. The software package DAS6 was provided by IBH Consultants Ltd. The fitting function used is

$$I(t) = b + \sum_j a_j e^{(-t/\tau j)} \quad (1)$$

The relative amplitude, also known as the fractional intensity, and the average fluorescence lifetime are calculated according to the following equations

$$f_i = a_i\tau_i / \sum_j a_j\tau_j \qquad \tau_{av} = \sum_j f_j\tau_j$$

4.10. Atomic Force Microscopy (AFM) and Kelvin Probe Force Microscopy (KPFM). Topography atomic force microscopy (AFM) and Kelvin probe force microscopy (KPFM) images have been realized employing a Multimode 8 (Bruker) microscope operated in air, employing Pt/Ir-coated cantilever-doped silicon tips (SCM-PIT-V2, Bruker), with mechanical constant k = 3 N/m and oscillating frequency f_0 ~75 kHz. Images are acquired by the two-passages mode: for every scan line, first, the topography is measured in tapping mode, and then the same line is rescanned at a lift height of ~50 nm, using amplitude modulation (AM) feedback. Kelvin probe force microscopy is a noninvasive technique probing the sample surface potential (SP) with nanoscale lateral resolution. SP can be related to the sample work function through the formula $|WF_{sample}| = |WF_{tip}| - SP$, where WF_{tip} is the tip work function, which can be easily calibrated by using a standard reference sample.

4.11. Macroscopic Kelvin Probe (KP). For the light illumination, we used a quartz halogen lamp (intensity <0.6 mW/mm^2) and measured the changes in the surface potential value when the light was switched on/off (interval time ~30 s). Samples of pristine fibers, pseudomorphic fibers (totally or partially treated with HOF·CH_3CN), and T8S4O8 were analyzed.

4.12. Single Crystal Conductivity. The electrical characterization was carried out on the crystalline fibers in vacuum (base pressure $p = 8 \times 10^{-5}$ mbar) on a wide temperature range (T = 300–40 K). The fibers, both treated and untreated, were carefully selected in size (length ~500 μm, wide ~15 μm, height ~15 μm, section area = 15 × 15 μm^2 = 2.25 × 10^{-6} cm^2) and shape, and transversally mounted onto two Ag electrodes evaporated on glass (Ag thickness 300 nm) separated by a 100 μm wide channel. Pseudomorphic fibers were picked up from samples of T8S4 fibers grown on glass (area 4 cm^2) and treated with 100 μL of HOF·CH_3CN leading to an oxidized shell thickness of about 100 nm. A good electrical contact between fiber and electrodes was ensured by mechanically pressing a thin (<3 mm) block of freshly prepared transparent and electrically insulating Poly(dimethylsiloxane) (PDMS) deposited on the top of the fiber. Longitudinal electrical conductivity was determined, in a two-contact mode, by applying a bias across the two bridging electrodes. The temperature-dependent conductivity of both pristine and pseudomorphized fibers was assessed by measuring the flowing current in fiber samples over the temperature range from 300 to 40 K. The conductivity of individual fibers was calculated by applying the formula

$$\sigma = \frac{1}{R} \cdot \frac{l}{A}$$

where, R is the measured resistance, l is the length spanned between the two electrodes, and A is the area of the fibers section.

Irradiation experiments were performed by using a CollLED pe-300lite light source coupled to a 3 mm liquid light guide. Output power at the end of the light guide measured with an Ophir Nova II power meter equipped with a PD300UV is 180 mW at 365 nm, 170 mW at 465 nm, and 105 mW at 560 nm (resulting on the fiber 3.8 × 10^{-2}, 3.6 × 10^{-2}, and 2.2 × 10^{-2} mW, respectively).

ASSOCIATED CONTENT

Supporting Information

The Supporting Information is available free of charge at https://pubs.acs.org/doi/10.1021/acsnano.4c11681.

Synthesis of T8S4O8 in solution; ^{1}H- and ^{13}C NMR spectra of T8S4O8; TLC and mass spectra of dissolved pseudomorphic fibers; characterization of T8S4O8; optical and SEM microscopy; XPS and XRD measurements; fibers' pseudomorphization attempts with H_2O_2; self-assembly of T8S4O8; DFT calculations of homo- and heterodimers; optical properties of fibers before and after HOF·CH_3CN treatment and T8S4O8 crystals; confocal fluorescence imaging; cyclic voltammetry; AFM, KP, and KPFM measurements; electrical measurements. (DOCX)

AUTHOR INFORMATION

Corresponding Authors

Massimo Baroncini − *Consiglio Nazionale delle Ricerche (CNR) − Istituto per la Sintesi Organica e la Fotoreattività (ISOF), 40129 Bologna, Italy; CLAN − Center for Light Activated Nanostructures, c/o ISOF-CNR, 40129 Bologna, Italy; Dipartimento di Scienze e Tecnologie Agro-alimentari, Università di Bologna, 40127 Bologna, Italy;* orcid.org/0000-0002-8112-8916; Email: massimo.baroncini@unibo.it

Francesca Di Maria − *Consiglio Nazionale delle Ricerche (CNR) − Istituto per la Sintesi Organica e la Fotoreattività (ISOF), 40129 Bologna, Italy; CLAN − Center for Light Activated Nanostructures, c/o ISOF-CNR, 40129 Bologna, Italy;* orcid.org/0000-0001-5557-3816; Email: francesca.dimaria@isof.cnr.it

Authors

Mattia Zangoli − *Consiglio Nazionale delle Ricerche (CNR) − Istituto per la Sintesi Organica e la Fotoreattività (ISOF), 40129 Bologna, Italy; CLAN − Center for Light Activated Nanostructures, c/o ISOF-CNR, 40129 Bologna, Italy;* orcid.org/0000-0002-0340-9245

Raffaello Mazzaro − *Dipartimento di Fisica e Astronomia "Augusto Righi", University of Bologna, 40127 Bologna, Italy; Consiglio Nazionale delle Ricerche (CNR) − Istituto*

https://doi.org/10.1021/acsnano.4c11681
ACS Nano XXXX, XXX, XXX−XXX

per la Microelettronica e i Microsistemi (IMM), 40129 Bologna, Italy; orcid.org/0000-0003-4598-9556

Eugenio Lunedei − *Consiglio Nazionale delle Ricerche (CNR) − Istituto per lo Studio dei Materiali Nanostrutturati (ISMN), 40129 Bologna, Italy;* orcid.org/0000-0002-2666-2577

Eduardo Fabiano − *Istituto per la Microelettronica e Microsistemi (CNR-IMM), c/o Campus Ecotekne, 73100 Lecce, Italy; Centre for Biomolecular Nanotechnologies @ UNILE, Istituto Italiano di Tecnologia (IIT), 73010 Lecce, Italy;* orcid.org/0000-0002-3990-669X

Ilse Manet − *Consiglio Nazionale delle Ricerche (CNR) − Istituto per la Sintesi Organica e la Fotoreattività (ISOF), 40129 Bologna, Italy;* orcid.org/0000-0002-8789-358X

Andrea Candini − *Consiglio Nazionale delle Ricerche (CNR) − Istituto per la Sintesi Organica e la Fotoreattività (ISOF), 40129 Bologna, Italy; CLAN − Center for Light Activated Nanostructures, c/o ISOF-CNR, 40129 Bologna, Italy;* orcid.org/0000-0003-3909-473X

Alessandro Kovtun − *Consiglio Nazionale delle Ricerche (CNR) − Istituto per la Sintesi Organica e la Fotoreattività (ISOF), 40129 Bologna, Italy;* orcid.org/0000-0002-7614-7100

Meriem Goudjil − *Consiglio Nazionale delle Ricerche (CNR) − Istituto per lo Studio dei Materiali Nanostrutturati (ISMN), 40129 Bologna, Italy;* Present Address: Dipartimento di Ingegneria Industriale, Università degli Studi di Firenze, via Santa Marta 3, 50139 Firenze, Italy; orcid.org/0000-0003-3401-4294

Alberto Zanelli − *Consiglio Nazionale delle Ricerche (CNR) − Istituto per la Sintesi Organica e la Fotoreattività (ISOF), 40129 Bologna, Italy;* orcid.org/0000-0001-8799-7998

Shlomo Rozen − *School of Chemistry, Tel-Aviv University, 69978 Tel Aviv, Israel;* orcid.org/0000-0002-8034-9530

Massimo Gazzano − *Consiglio Nazionale delle Ricerche (CNR) − Istituto per la Sintesi Organica e la Fotoreattività (ISOF), 40129 Bologna, Italy;* orcid.org/0000-0003-1352-9547

Complete contact information is available at: https://pubs.acs.org/10.1021/acsnano.4c11681

Author Contributions

[¶]M.Z., R.M., and E.L. contributed equally to this work. M.Z., M.B., F.D.M. synthesized and characterized the materials. R.M. carried out SEM experiments. E.L. and M.G. performed microspectroscopy and electrical measurements. E.F. performed theoretical calculations. I.M. performed LSCM measurements. A.C. carried out KPFM analysis. M.G. collected XRD data. A.K. performed XPS measurements. M.B. and F.D.M. designed the study and wrote the manuscript. F.D.M. conceived the original idea and supervised the project. All authors critically discussed the data and manuscript and approved the final version.

Notes

The authors declare no competing financial interest.

ACKNOWLEDGMENTS

M.Z. and F.D.M. acknowledge project LiveSens (Air Force Office of Scientific Research (AFOSR) Projects: FA8655-22-1-7014). M.Z., M.B., and F.D.M. acknowledge the PRIN project EMBRACE (IntErLocked supraMolecular assemBlies in solution: the access key to new donoR−Acceptor multi-Component architEctures, CUP Number: B53D23015460006).

DEDICATION

Dedicated to Giovanna Barbarella.

REFERENCES

(1) Rajeshwar, K.; Tacconi, N. R.; Chenthamarakshan, C. R. Semiconductor-Based Composite Materials: Preparation, Properties, and Performance. *Chem. Mater.* **2001**, *13*, 2765−2782.

(2) Gao, W.; Reis, R.; Schelhas, L. T.; Pool, V. L.; Toney, M. F.; Yu, K. M.; Walukiewicz, W. Formation of Nanoscale Composites of Compound Semiconductors Driven by Charge Transfer. *Nano Lett.* **2016**, *16*, 5247−5254.

(3) Kamat, P. V.; Tvrdy, K.; Baker, D. R.; Radich, E. J. Beyond Photovoltaics: Semiconductor Nanoarchitectures for Liquid-Junction Solar Cells. *Chem. Rev.* **2010**, *110*, 6664−6688.

(4) Song, H.; Lin, Y.; Zhang, Z.; Rao, H.; Wang, W.; Fang, Y.; Pan, Z.; Zhong, X. Improving the Efficiency of Quantum Dot Sensitized Solar Cells beyond 15% via Secondary Deposition. *J. Am. Chem. Soc.* **2021**, *143*, 4790−4800.

(5) Bhattacharya, S.; Samanta, S. K. Soft-Nanocomposites of Nanoparticles and Nanocarbons with Supramolecular and Polymer Gels and Their Applications. *Chem. Rev.* **2016**, *116*, 11967−12028.

(6) Wang, Y.; Chen, K.-L.; Prine, N.; Rondeau-Gagné, S.; Chiu, Y.-C.; Gu, X. Stretchable and Self-Healable Semiconductive Composites Based on Hydrogen Bonding Cross-linked Elastomeric Matrix. *Adv. Funct. Mater.* **2023**, *33*, No. 2303031.

(7) Putnis, A. *An Introduction to Mineral Sciences*; Cambridge University Press, 1992.

(8) Putnis, A. Mineral replacement reactions: from macroscopic observations to microscopic mechanisms. *Mineral. Mag.* **2002**, *66*, 689−708.

(9) Putnis, A. Mineral Replacement Reactions. *Rev. Mineral. Geochem.* **2009**, *70*, 87−124.

(10) Roza-Llera, A.; Jiménez, A.; Fernández-Díaz, L. Mechanism and kinetics of the pseudomorphic replacement of anhydrite by calcium phosphate phases at hydrothermal conditions. *Am. Mineral.* **2023**, *108*, 1708−1719.

(11) Ruiz-Agudo, E.; Putnis, C. V.; Putnis, A. Coupled dissolution and precipitation at mineral−fluid interfaces. *Chem. Geol.* **2014**, *383*, 132−146.

(12) González-Illanes, T.; Borrero, M. T.; Herráez, M. M.; Pimentel, C.; Pina, C. M. Pseudomorphic Replacement of Mg−Ca Carbonates after Gypsum and Anhydrite. *ACS Earth Space Chem.* **2017**, *1*, 168−178.

(13) Bilo, M.; Münzner, M.; Küster, C.; Enke, D.; Lee, Y. J.; Fröba, M. Structural Changes of Hierarchically Nanoporous Organosilica/Silica Hybrid Materials by Pseudomorphic Transformation. *Chem. − Eur. J.* **2020**, *26*, 11220−11230.

(14) Lytle, J. C.; Yan, H.; Turgeon, R. T.; Stein, A. Multistep, Low-Temperature Pseudomorphic Transformations of Nanostructured Silica to Titania via a Titanium Oxyfluoride Intermediate. *Chem. Mater.* **2004**, *16*, 3829−3837.

(15) Martin, T.; Galarneau, A.; Di Renzo, F.; Fajula, F.; Plee, D. Morphological Control of MCM-41 by Pseudomorphic Synthesis. *Angew. Chem., Int. Ed.* **2002**, *41*, 2590−2592.

(16) Galarneau, A.; Iapichella, J.; Bonhomme, K.; Di Renzo, F.; Kooyman, P.; Terasaki, O.; Fajula, F. Controlling the Morphology of Mesostructured Silicas by Pseudomorphic Transformation: a Route Towards Applications. *Adv. Funct. Mater.* **2006**, *16*, 1657−1667.

(17) Lim, W. Y.; Lim, Y. F.; Ho, G. W. Pseudomorphic-phase transformation of NiCo based ternary hierarchical 2D-1D nanostructures for enhanced electrocatalysis. *J. Mater. Chem. A* **2017**, *5*, 919−924.

(18) Reboul, J.; Furukawa, S.; Horike, N.; Tsotsalas, M.; Hirai, K.; Uehara, H.; Kondo, M.; Louvain, N.; Sakata, O.; Kitagawa, S.

Mesoscopic architectures of porous coordination polymers fabricated by pseudomorphic replication. *Nat. Mater.* **2012**, *11*, 717−723.
(19) Shao, L.; Fan, F.; Dai, X.; Fu, H.; Li, W.; Qi, W.; Meng, F. B.; Fu, Y. Pseudomorphic Replacement in the Transformation between Metal−Organic Frameworks toward Three-Dimensional Hierarchical Nanostructures. *Chem. Mater.* **2022**, *34*, 5356−5365.
(20) Yilmaz, G.; Yam, K. M.; Zhang, C.; Fan, H. J.; Ho, G. W. In Situ Transformation of MOFs into Layered Double Hydroxide Embedded Metal Sulfides for Improved Electrocatalytic and Supercapacitive Performance. *Adv. Mater.* **2017**, *29*, No. 1606814.
(21) Liu, Z.; Navas, J. L.; Han, W.; Ibarra, M. R.; Kwan, J. K. C.; Yeung, K. L. Gel transformation as a general strategy for fabrication of highly porous multiscale MOF architectures. *Chem. Sci.* **2023**, *14*, 7114−7125.
(22) Chen, J.; Zhuang, P.; Ge, Y.; Chu, H.; Yao, L.; Cao, Y.; Wang, Z.; Chee, M. O. L.; Dong, P.; Shen, J.; Ye, M.; Ajayan, P. M. Sublimation-Vapor Phase Pseudomorphic Transformation of Template-Directed MOFs for Efficient Oxygen Evolution Reaction. *Adv. Funct. Mater.* **2019**, *29*, No. 1903875.
(23) Perepichka, I. F.; Perepichka, D. F. *Handbook of Thiophene-Based Materials: Applications in Organic Electronics and Photonics*; John Wiley & Sons, Ltd., 2009.
(24) Barbarella, G.; Zangoli, M.; Di Maria, F. Chapter Three - Synthesis and Applications of Thiophene Derivatives as Organic Materials. *Adv. Heterocycl. Chem.* **2017**, *123*, 105−167.
(25) Ding, L.; Yu, Z. D.; Wang, X. Y.; Yao, Z. F.; Lu, Y.; Yang, C. Y.; Wang, J. Y.; Pei, J. Polymer Semiconductors: Synthesis, Processing, and Applications. *Chem. Rev.* **2023**, *123*, 7421−7497.
(26) Wei, S.; Xia, J.; Dell, E. J.; Jiang, Y.; Song, R.; Lee, H.; Rodenbough, P.; Briseno, A. L.; Campos, L. M. Bandgap Engineering through Controlled Oxidation of Polythiophenes. *Angew. Chem.* **2014**, *126*, 1863−1867.
(27) Di Maria, F.; Zanelli, A.; Liscio, A.; Kovtun, A.; Salatelli, E.; Mazzaro, R.; Morandi, V.; Bergamini, G.; Shaffer, A.; Rozen, S. Poly(3-hexylthiophene) Nanoparticles Containing Thiophene-S,S-dioxide: Tuning of Dimensions, Optical and Redox Properties, and Charge Separation under Illumination. *ACS Nano* **2017**, *11*, 1991−1999.
(28) Rozen, S. HOF·CH3CN: Probably the Best Oxygen Transfer Agent Organic Chemistry Has To Offer. *Acc. Chem. Res.* **2014**, *47*, 2378−2389.
(29) Rozen, S.; Bareket, Y. Oxidation of Sulfur-Containing Compounds with HOF·CH3CN. *J. Org. Chem.* **1997**, *62*, 1457−1462.
(30) Potash, S.; Rozen, S. New Conjugated Oligothiophenes Containing the Unique Arrangement of Internal Adjacent [All]-S,S-Oxygenated Thiophene Fragments. *Chem. − Eur. J.* **2013**, *19*, 5289−5296.
(31) Di Maria, F.; Zangoli, M.; Palamá, I. E.; Fabiano, E.; Zanelli, A.; Monari, M.; Perinot, A.; Caironi, M.; Maiorano, V.; Maggiore, A.; Pugliese, M.; Salatelli, E.; Gigli, G.; Viola, I.; Barbarella, G. Improving the Property−Function Tuning Range of Thiophene Materials via Facile Synthesis of Oligo/Polythiophene-S-Oxides and Mixed Oligo/Polythiophene-S-Oxides/Oligo/Polythiophene-S,S-Dioxides. *Adv. Funct. Mater.* **2016**, *26*, 6970−6984.
(32) Barsotti, J.; Perotto, S.; Candini, A.; Colombo, E.; Camargo, F. V. A.; Di Marco, S.; Zangoli, M.; Sardar, S.; Barker, A. J.; D'Andrea, C.; Cerullo, G.; Rozen, S.; Benfenati, F.; Di Maria, F.; Lanzani, G. Core−Shell Architecture in Poly(3-hexylthiophene) Nanoparticles: Tuning of the Photophysical Properties for Enhanced Neuronal Photostimulation. *ACS Appl. Mater. Interfaces* **2023**, *15*, 13472−13483.
(33) Zangoli, M.; Cantelli, A.; Candini, A.; Lewinska, A.; Fardella, F.; Tino, A.; Tommasini, G.; Wnuk, M.; Moschetta, M.; Perotto, S.; Lucarini, M.; Tortiglione, C.; Lanzani, G.; Di Maria, F. Photoreactivity of Thiophene-Based Core@Shell Nanoparticles: The Effect of Photoinduced Charge Separation on In Vivo ROS Production. *J. Phys. Chem. C* **2023**, *127*, 4672−4683.
(34) Di Maria, F.; Olivelli, P.; Gazzano, M.; Zanelli, A.; Biasiucci, M.; Gigli, G.; Gentili, D.; D'Angelo, P.; Cavallini, M.; Barbarella, G. A Successful Chemical Strategy To Induce Oligothiophene Self-Assembly into Fibers with Tunable Shape and Function. *J. Am. Chem. Soc.* **2011**, *133*, 8654−8661.
(35) Gentili, D.; Di Maria, F.; Liscio, F.; Ferlauto, L.; Leonardi, F.; Maini, L.; Gazzano, M.; Milita, S.; Barbarella, G.; Cavallini, M. Targeting ordered oligothiophene fibers with enhanced functional properties by interplay of self-assembly and wet lithography. *J. Mater. Chem.* **2012**, *22*, 20852−20856.
(36) Di Maria, F.; Fabiano, E.; Gentili, D.; Biasiucci, M.; Salzillo, T.; Bergamini, G.; Gazzano, M.; Zanelli, A.; Brillante, A.; Cavallini, M.; Della Sala, F.; Gigli, G.; Barbarella, G. Polymorphism in Crystalline Microfibers of Achiral Octithiophene: The Effect on Charge Transport, Supramolecular Chirality and Optical Properties. *Adv. Funct. Mater.* **2014**, *24*, 4943−4951.
(37) Di Maria, F.; Zangoli, M.; Gazzano, M.; Fabiano, E.; Gentili, D.; Zanelli, A.; Fermi, A.; Bergamini, G.; Bonifazi, D.; Perinot, A.; Caironi, M.; Mazzaro, R.; Morandi, V.; Gigli, G.; Liscio, A.; Barbarella, G. Controlling the Functional Properties of Oligothiophene Crystalline Nano/Microfibers via Tailoring of the Self-Assembling Molecular Precursors. *Adv. Funct. Mater.* **2018**, *28*, No. 1801946.
(38) Zangoli, M.; Di Maria, F.; Barbarella, G. Supramolecular Assembly of Thiophene-Based Oligomers into Nanostructured Fluorescent Conductive and Chiral Microfibers. *ChemistryOpen* **2020**, *9*, 499−511.
(39) Pedrosa, E. T.; Putnis, C. V.; Renard, F.; Burgos-Cara, A.; Laurich, B.; Putnis, A. Porosity generated during the fluid-mediated replacement of calcite by fluorite. *CrystEngComm* **2016**, *18*, 6867−6874.
(40) Contreras-García, J.; Johnson, E. R.; Keinan, S.; Chaudret, R.; Piquemal, J. P.; Beratan, D. N.; Yang, W. NCIPLOT: A Program for Plotting Noncovalent Interaction Regions. *J. Chem. Theory Comput.* **2011**, *7*, 625−632.
(41) Contreras-García, J.; Yang, W.; Johnson, E. R. Analysis of Hydrogen-Bond Interaction Potentials from the Electron Density: Integration of Noncovalent Interaction Regions. *J. Phys. Chem. A* **2011**, *115*, 12983−12990.
(42) Guerraoui, A.; Goudjil, M.; Direm, A.; Guerraoui, A.; Sengün, I. Y.; Parlak, C.; Djedouani, A.; Chelazzi, L.; Monti, F.; Lunedei, E.; Boumaza, A. A rhodanine derivative as a potential antibacterial and anticancer agent: Crystal structure, spectral characterization, DFT calculations, Hirshfeld surface analysis, in silico molecular docking and ADMET studies. *J. Mol. Struct.* **2023**, *1280*, No. 135025.
(43) Li, X.; Zhang, Q.; Yu, J.; Xu, Y.; Zhang, R.; Wang, C.; Zhang, H.; Fabiano, S.; Liu, X.; Hou, J.; Gao, F.; Fahlman, M. Mapping the energy level alignment at donor/acceptor interfaces in non-fullerene organic solar cells. *Nat. Commun.* **2022**, *13*, No. 2046.
(44) Karuthedath, S.; Gorenflot, J.; Firdaus, Y.; Chaturvedi, N.; De Castro, C. S. P.; Harrison, G. T.; Khan, J. I.; Markina, A.; Balawi, A. H.; Dela Peña, T. A.; Liu, W.; Liang, R. Z.; Sharma, A.; Paleti, S. H. K.; Zhang, W.; Lin, Y.; Alarousu, E.; Lopatin, S.; Anjum, D. H.; Anjum, D. H.; Beaujuge, P. M.; Beaujuge, P. M.; Wolf, S.; De Wolf, S.; McCulloch, I.; McCulloch, I.; Anthopoulos, T. D.; Anthopoulos, T. D.; Baran, D.; Baran, D.; Andrienko, D.; Andrienko, D.; Laquai, F. Intrinsic efficiency limits in low-bandgap non-fullerene acceptor organic solar cells. *Nat. Mater.* **2021**, *20*, 378−384.
(45) Neusser, D.; Sun, B.; Tan, W. L.; Thomsen, L.; Schultz, T.; Perdigón-Toro, L.; Koch, N.; Shoaee, S.; McNeill, C. R.; Neher, D.; Ludwigs, S.; Perdigón Toro, L.; Koch, N.; Shoaee, S.; McNeill, C. R.; Neher, D.; Ludwigs, S. Spectroelectrochemically determined energy levels of PM6:Y6 blends and their relevance to solar cell performance. *J. Mater. Chem. C* **2022**, *10*, 11565−11578.
(46) Melitz, W.; Shen, J.; Kummel, A. C.; Lee, S. Kelvin probe force microscopy and its application. *Surf. Sci. Rep.* **2011**, *66*, 1−27.
(47) Baikie, I. D.; Mackenzie, S.; Estrup, P. J. Z.; Meyer, J. A. Kelvin probe error compensation based on harmonic analysis of measurement signal. *Rev. Sci. Instrum.* **1991**, *62*, 1326−1332.
(48) Liscio, A.; Palermo, E.; Fenwick, O.; Braun, S.; Mullen, K.; Fahlman, M.; Cacialli, F.; Samorì, P. Local Surface Potential of π-

https://doi.org/10.1021/acsnano.4c11681
ACS Nano XXXX, XXX, XXX−XXX

Conjugated Nanostructures by Kelvin Probe Force Microscopy: Effect of the Sampling Depth. *Small* **2011**, *7*, 634−639.
(49) Zhou, N.; Wang, R.; Zhou, X.; Song, H.; Xiong, X.; Ding, Y.; Lü, J.; Gan, L.; Zhai, T. P-GaSe/N-MoS2 Vertical Heterostructures Synthesized by van der Waals Epitaxy for Photoresponse Modulation. *Small* **2018**, *14*, No. 1702731.
(50) Wu, F.; Li, Q.; Wang, P.; Xia, H.; Wang, Z.; Wang, Y.; Luo, M.; Chen, L.; Chen, F.; Miao, J.; Chen, X.; Lu, W.; Shan, C.; Pan, A.; Wu, X.; Ren, W.; Jariwala, D.; Hu, W. High efficiency and fast van der Waals hetero-photodiodes with a unilateral depletion region. *Nat. Commun.* **2019**, *10*, No. 4663.
(51) Minj, A.; Cros, A.; Auzelle, T.; Pernot, J.; Daudin, B. Direct assessment of p−n junctions in single GaN nanowires by Kelvin probe force microscopy. *Nanotechnology* **2016**, *27*, No. 385202.
(52) Ghani, F.; Opitz, A.; Pingel, P.; Heimel, G.; Salzmann, I.; Frisch, J.; Neher, D.; Tsami, A.; Scherf, U.; Koch, N. Charge transfer in and conductivity of molecularly doped thiophene-based copolymers. *J. Polym. Sci., Part B: Polym. Phys.* **2015**, *53*, 58−63.
(53) Pingel, P.; Zhu, L.; Park, K. S.; Vogel, J. O.; Janietz, S.; Kim, E. G.; Rabe, J. P.; Brédas, J. L.; Koch, N. Charge-Transfer Localization in Molecularly Doped Thiophene-Based Donor Polymers. *J. Phys. Chem. Lett.* **2010**, *1*, 2037−2041.
(54) Lüssem, B.; Riede, M.; Leo, K. Doping of organic semiconductors. *Phys. Status Solidi A* **2013**, *210*, 9−43.
(55) Scaccabarozzi, A. D.; Basu, A.; Aniés, F.; Liu, J.; Zapata-Arteaga, O.; Warren, R.; Firdaus, Y.; Nugraha, M. I.; Lin, Y.; Campoy-Quiles, M.; Koch, N.; Müller, C.; Tsetseris, L.; Heeney, M.; Anthopoulos, T. D. Doping Approaches for Organic Semiconductors. *Chem. Rev.* **2022**, *122*, 4420−4492.
(56) Salzmann, I.; Heimel, G.; Oehzelt, M.; Winkler, S.; Koch, N. Molecular Electrical Doping of Organic Semiconductors: Fundamental Mechanisms and Emerging Dopant Design Rules. *Acc. Chem. Res.* **2016**, *49*, 370−378.
(57) Fichou, D. *Handbook of Oligo- and Polythiophenes*; Wiley-VCH Verlag GmbH, 1998.
(58) Möller, S.; Perlov, C.; Jackson, W.; Taussig, C.; Forrest, S. R. A polymer/semiconductor write-once read-many-times memory. *Nature* **2003**, *426*, 166−169.
(59) Filapek, M.; Hellwig, H.; Gancarz, P.; Szłapa-Kula, A. Influence of Various Doping Agents on Organic Semiconductors' Physicochemical Properties. *J. Electrochem. Soc.* **2021**, *168*, No. 046508.
(60) Dutta, S.; Narayan, K. S. Gate-Voltage Control of Optically-Induced Charges and Memory Effects in Polymer Field-Effect Transistors. *Adv. Mater.* **2004**, *16*, 2151−2155.
(61) Narayan, K. S.; Kumar, N. Light responsive polymer field-effect transistor. *Appl. Phys. Lett.* **2001**, *79*, 1891−1893.
(62) Chen, W. C. *Electrical Memory Materials and Devices*; RSC, 2015.
(63) Perdew, J. P.; Ernzerhof, M.; Burke, K. Rationale for mixing exact exchange with density functional approximations. *J. Chem. Phys.* **1996**, *105*, 9982−9985.
(64) Weigend, F.; Ahlrichs, R. Balanced basis sets of split valence, triple zeta valence and quadruple zeta valence quality for H to Rn: Design and assessment of accuracy. *Phys. Chem. Chem. Phys.* **2005**, *7*, 3297−3305.
(65) Franzke, Y. J.; Holzer, C.; Andersen, J. H.; Begušić, T.; Bruder, F.; Coriani, S.; Della Sala, F.; Fabiano, E.; Fedotov, D. A.; Fürst, S.; Gillhuber, S.; Grotjahn, R.; Kaupp, M.; Kehry, M.; Krstić, M.; Mack, F.; Majumdar, S.; Nguyen, B. D.; Parker, S. M.; Pauly, F.; Pausch, A.; Perlt, E.; Phun, G. S.; Rajabi, A.; Rappoport, D.; Samal, B.; Schrader, T.; Sharma, M.; Tapavicza, E.; Treß, R. S.; Voora, V.; Wodyński, A.; Yu, J. M.; Zerulla, B.; Furche, F.; Hättig, C.; Sierka, M.; Tew, D. P.; Weigend, F. TURBOMOLE: Today and Tomorrow. *J. Chem. Theory Comput.* **2023**, *19*, 6859.
(66) Perdew, J. P.; Burke, K.; Ernzerhof, M. Generalized Gradient Approximation Made Simple. *Phys. Rev. Lett.* **1996**, *77*, 3865−3868.

https://doi.org/10.1021/acsnano.4c11681
ACS Nano XXXX, XXX, XXX−XXX